

QSO METAL ABSORPTION SYSTEMS AT HIGH REDSHIFT AND THE SIGNATURE OF HIERARCHICAL GALAXY FORMATION

MICHAEL RAUCH,^{1,2} MARTIN G. HAEHNELT,³ AND MATTHIAS STEINMETZ^{3,4}
mr@astro.caltech.edu, mhaehnelt@mpa-garching.mpg.de, msteinmetz@astro.berkeley.edu

Received 1996 September 3; accepted 1996 December 26

ABSTRACT

In a hierarchical cosmogony, galaxies build up by continuous merging of smaller structures. At $z = 3$, the matter content of a typical present-day galaxy is dispersed over several individual clumps embedded in sheetlike structures, often aligned along filaments. We have used hydrodynamical simulations to investigate the spatial distribution and absorption properties of metal-enriched gas in such regions of ongoing galaxy formation. The metal and hydrogen absorption features produced by the collapsing structures closely resemble observed QSO absorption systems over a wide range in H I column density. Strong C II and Si IV absorption occurs for lines of sight passing the densest regions close to the center of the protogalactic clumps, while C IV is a good tracer of the prominent filamentary structures and O VI becomes the strongest absorption feature for lines of sight passing through low-density regions far away from fully collapsed objects. The observed column density ratios of the different ionic species at $z = 3$ can be well reproduced if a mean metallicity $[Z/H] = -2.5$, relative abundances as found in metal-poor stars, a UV background with intensity $J_{-22} = 3$ at the Lyman limit, and either a power-law spectrum ($J \propto \nu^{-1.5}$) or the spectral shape proposed by Haardt & Madau are assumed. The observed scatter in $[C/H]$ is about a magnitude larger than that in the simulations, which suggests an inhomogeneous metal distribution. Observed and simulated Doppler parameter distributions of H I and C IV absorption lines are in good agreement, which indicates that shock heating due to gravitational collapse is a second important heating agent in addition to photoionization heating. The large velocity spreads seen in some C IV systems may be due to the occasional alignments of the observer's line of sight with expanding large-scale filaments. Both high-ionization multicomponent heavy-element absorbers and damped Ly α systems can arise from groups of moderately sized protogalactic clumps ($M_{\text{baryon}} \sim 10^9 M_{\odot}$). Recent detections of star-forming galaxies at similar redshifts are consistent with this picture.

Subject headings: galaxies: formation — hydrodynamics — quasars: absorption lines

1. INTRODUCTION

Can we understand galaxy formation at high redshift studying QSO absorption systems? Lines of sight (LOS) to distant QSOs must frequently traverse protogalactic environments. If the gas in these regions has already experienced some metal enrichment, the galaxy formation process should produce a characteristic pattern of metal absorption lines in the QSO spectrum. If we succeed in identifying the spectroscopic signature of such regions, high-resolution spectra of QSOs at high redshift should be able to yield detailed insights into the physical state of the gas in young galaxies and the gaseous reservoir from which they form. Once the observable absorption features have been related to the properties of the absorbing objects, one may hope to be able actually to constrain the galaxy formation process and cosmological parameters. This paper is mostly concerned with the first aspect: what *are* absorption systems (in particular: heavy element systems) at high redshift, and can we model them realistically by adopting a specific scenario of structure formation?

QSO absorption studies provide only one-dimensional information, so observations of single LOS cannot give independently the spatial density and the size of the objects causing the absorption. Only the product of number density

and cross section is constrained. Additional information about the spatial distribution of the absorbing gas has to be sought, e.g., by the identification of heavy element absorbers with a class of galaxies whose number density is known. As Bahcall & Spitzer (1969) and Burbidge et al. (1977) pointed out, the cross section of the absorbing gas would have to be much larger than typical half-light radii of present-day spiral galaxies if these objects had the same comoving space density as such galaxies. First observational evidence in favor of large metal absorption cross sections came from work by Bergeron (1986) who discovered low-redshift galaxies close to the LOS to QSOs with known Mg II absorption systems, coincident in redshift with the absorbers. Surveys of optically thick (Lyman limit) absorption systems and galaxies at intermediate redshift have reported results consistent with galaxies being surrounded by Mg II absorbing halos of radius ~ 40 kpc (see, e.g., Bergeron 1995; Steidel 1995; Churchill, Steidel, & Vogt 1996). Extending such work to optically thin systems and lower redshifts, Lanzetta et al. (1995) found evidence for even larger H I halos with radii of order 160 kpc. Similarly, damped Ly α systems were interpreted by Wolfe and collaborators (see, e.g., Wolfe 1988; Lanzetta et al. 1991) as large protodisks, progenitors of present-day spiral galaxies with significantly larger radii at high redshift.

The large-halo/disk scenario is able to explain qualitatively the ionization and component structure of heavy element absorption systems, especially the observations of low- and intermediate-redshift low-ionization Mg II systems, and perhaps also the strong clustering measured for C IV systems (Sargent et al. 1979; Sargent, Boksenberg,

¹ Astronomy Department, California Institute of Technology, Pasadena, CA 91125.

² Hubble Fellow.

³ Max-Planck-Institut für Astrophysik, Postfach 1523, 85740 Garching, Germany.

⁴ Department of Astronomy, University of California–Berkeley, Berkeley, CA 94720.

& Steidel 1988; Petitjean & Bergeron 1994). In this picture the individual absorption components are dense clouds pressure-confined by hot gas and orbiting in a large gravitationally bound halo or corotating in a disk. Such a two-phase medium could be produced, e.g., by thermal instability (Bahcall 1975; Fall & Rees 1985; Mo 1994). Mo & Miralda-Escudé (1996) investigated such a model in detail and found that the clouds responsible for Mg II and C IV should have a typical mass $\sim 10^6 M_\odot$ and radial extent ~ 1 kpc.

At high redshift, much less is known about the cross section of metal absorbers. Secure identifications of the absorbing objects with massive galaxies are currently restricted to low redshift. Nevertheless, large virialized objects have also been invoked, mainly from a heuristic point of view, to explain some of the characteristics of *high-redshift* ($z > 2$) absorbers (see, e.g., Wolfe 1988). Measurements of the sizes of damped Ly α absorbers at high redshift so far are rare and appear contradictory (see, e.g., Møller & Warren 1995; Djorgovski et al. 1996). *Large* disks are, however, not the only viable dynamical model for the observed velocity structure. Moreover, observations of galaxies at high redshift are strongly biased toward objects with high current star formation rates. Thus, it is not clear whether the transverse separations on the sky of galaxy-absorber pairs coincident in redshift do reliably indicate the presence and sizes of any large, coherent objects. It is difficult to ascertain that there is not an undetected (not necessarily faint) galaxy closer to the LOS.

The alternative possibility of “smaller” but more numerous objects as sources of the metal absorption has also been explored earlier. Tyson (1988) suggested identifying damped Ly α systems with gas-rich dwarf galaxies instead of large protodisks. York et al. (1986) discussed clusters of such objects to explain the component structure of C IV systems. Individual galaxy halos cannot produce potential wells deep enough to explain the largest velocity splittings of C IV systems (up to 1000 km s^{-1}) as virialized motions. Pettini et al. (1983) and Morris et al. (1986) concluded that the velocity splitting and large cross sections are equally difficult to understand if objects similar to present-day galaxy clusters placed at high redshift were causing the absorption.

Earlier attempts at understanding QSO absorption systems have mostly employed phenomenological models. The ionization state of the gas was calculated with simplified assumptions about the geometry, temperature, and dynamical structure of the gas. Recently, realistic hydrodynamical simulations of the fate of gas in a universe subject to hierarchical structure formation (Cen et al. 1994; Hernquist et al. 1996) have led to a better understanding of the large-scale distribution of baryons. In the new picture, a coherent filamentary large-scale structure of dark matter and baryons is responsible for Ly α forest absorption lines (see, e.g., Petitjean, Mucket, & Kates 1995; Zhang, Anninos, & Norman 1995; Miralda-Escudé et al. 1996). Denser condensations embedded in the filaments are unstable against rapid collapse and cooling of the gas and probably form stars at their centers. In such a hierarchical picture, gravitational clustering should play an increasing role in generating distinct absorption systems toward higher redshift (see Lake 1988). At high z , typical dark matter halos are smaller and more numerous than present-day galaxies. Simple scaling laws predict that for fixed circular velocity, both their mass and their radius decrease as $(1+z)^{-3/2}$ (see

Kauffmann 1996 and Steinmetz 1996a for quantitative predictions). Thus, typical damped Ly α systems are predicted to be significantly smaller (rather than larger) than spiral galaxies at the present (Kauffmann 1996).

If these ideas are correct, then a considerable fraction of the complexity seen in heavy element absorbers should arise from entire groups of smallish, protogalactic objects prior to merging, in addition to any structure from density variations internal to already virialized, i.e., hydrostatically or rotationally supported, objects. Current observations do not yet allow us to determine what the dominant contributors to the metal absorption systems are, but they are quite consistent with this picture:

1. Recent Keck spectroscopy of Ly α forest systems (Cowie et al. 1995; Tytler et al. 1995) has shown that contamination of Ly α forest clouds by carbon is common in high-redshift Ly α absorbers with H I column densities as low as a few times 10^{14} cm^{-2} . In the numerical simulations, such column densities typically correspond to gas densities smaller than those expected for fully collapsed objects at these redshifts (indicating baryonic overdensities of order 10), so at least some metal absorption systems may occur outside the region of full gravitational collapse.

2. Typical observed temperatures of C IV systems are somewhat larger than expected if the gas were heated only by photoionization (Rauch et al. 1996). Such an enhancement is predicted by numerical simulations (Haehnelt, Steinmetz, & Rauch 1996b, hereafter Paper I; Haehnelt, Rauch, & Steinmetz 1996a) and can be produced by shock and (to a smaller extent) adiabatic heating during the gravitational compression of the gas.

In Paper I we used numerical hydrodynamical simulations to demonstrate that observed C IV absorption systems can indeed be qualitatively understood in terms of absorption by “protogalactic clumps” (PGCs), i.e., small, future constituents of large galaxies, forming through gravitational instability in a hierarchical cosmogony. These objects have large enough masses and H I column densities to have formed stars and appear as an early generation of galaxies. The C IV and H I absorption features caused by groups of PGCs were found to resemble observed C IV and H I absorption systems if an overall homogeneous abundance of $[C/H] \approx -3$ to -2 was assumed.

Here, we will perform a quantitative analysis and extend the work to a larger set of diagnostically useful ionic species. Section 2 will give the details of the numerical modeling. In § 3 we discuss the line formation process and the physical nature of the absorbing structures in regions of ongoing galaxy formation. In § 4 we discuss the observational consequences. Conclusions are drawn in § 5. All analysis presented in the present paper is for simulations at $z = 3.07$.

2. NUMERICAL SIMULATIONS

2.1. The Code

The simulations were performed using GRAPESPH (Steinmetz 1996b). This code combines a direct summation N -body integrator with the smoothed particle hydrodynamics technique (Lucy 1977; Gingold & Monaghan 1977) and is implemented for the special-purpose hardware GRAPE (Sugimoto et al. 1990). The version of the code we use here is especially adapted to follow a mixture of collisionless (dark matter) and collisional (gas) fluids. It is fully

Lagrangian, three-dimensional, and highly adaptive in space and time as the result of the use of individual smoothing lengths and individual time steps. The physical processes included in this version of the code include self-gravity, pressure gradients, hydrodynamical shocks, radiative and Compton cooling, and photoheating by a UV background with a specified spectrum. We do not assume rate equilibrium for the dominant baryonic species (H, H⁺, He, He⁺, He⁺⁺, and e⁻) but follow self-consistently their nonequilibrium time evolution. However, this had only a modest effect on the gas temperature in the lowest density regions. The nonequilibrium time evolution can generally be neglected for the questions addressed in this paper but will be important for low column density systems at epochs close to reionization. We assume that the gas remains optically thin throughout the calculation and that the background radiation is uniform in space. Radiative transfer effects have been neglected (see also Navarro & Steinmetz 1997).

2.2. Initial Conditions

The initial conditions are identical to those in Navarro & Steinmetz (1997) and were originally designed to study the formation of galaxies with circular velocities between 80 and 200 km s⁻¹. The background cosmological model is a $\Omega = 1$, $H_0 = 50$ km s⁻¹ Mpc⁻¹ cold dark matter (CDM) universe with a normalization of $\sigma_8 = 0.63$. The baryon fraction is $\Omega_b = 0.05$. Based on a P³M large-scale structure simulation of collisionless dark matter in a 30 Mpc box, eight halos were selected (four each with circular velocity of about 100 km s⁻¹ and 200 km s⁻¹) at $z = 0$. The dark matter particles belonging to these halos are traced back from $z = 0$ to $z = 21$. The smallest spherical regions containing all the particles contributing to the future halos are then resimulated at much higher resolution. About 35,000 particles are placed in spheres of radius 2.3 (3.8) Mpc (comoving) for the systems with a circular velocity of 100 km s⁻¹ (200 km s⁻¹). The particle mass was $4.9 \times 10^6 M_\odot$ and $2.3 \times 10^7 M_\odot$ in the low- and high-mass systems, respectively. The particles within the high-resolution sphere are perturbed with the same long waves as in the original P³M simulation. Additional short-wavelength modes up to the Nyquist frequency of the refined particle distribution are added on a 40³ grid with a linear extent corresponding to the diameter of the high-resolution sphere. About 1200 additional particles of higher mass outside the high-resolution sphere represent the tidal field of the surrounding matter. We adopt a Plummer gravitational softening of 2.5 (5) kpc for the dark matter and of 1.25 (2.5) kpc for the gas particles in the low- (high-) mass systems. All high-resolution runs are started at $z = 21$. At smaller redshifts, the high-resolution region is tidally distorted. At $z = 3$, these distortions are, however, still rather small ($\approx 10\%$ – 20% in the axis ratios).

We use several different descriptions for the intensity, redshift dependence, and frequency dependence of the UV background. Most of the simulations were done using a power-law spectral energy distribution and the redshift dependence suggested by Vedel, Hellsten, & Sommer-Larsen (1994). We varied turn-on redshift, spectral index ($\alpha = 1 \dots 2$) and normalization of the background ($J_{-22} = 0.3 \dots 30$, in units of 10^{-22} ergs s⁻¹ cm⁻² Hz⁻¹ sr⁻¹). The more realistic description of the UV background proposed by Haardt & Madau (1996) was also used. Although

varying the UV background had noticeable effects on the temperature and the ionization of the gas, the effects on the overall gas distribution were small. In this paper we will discuss these effects only briefly and will concentrate on simulations with $\alpha = 1.5$ and $J_{-22} = 3$ for which the background was switched on at the beginning of the simulation ($z = 21$). This corresponds to a typical quasar-like spectrum and is consistent with measurements of the helium Gunn-Peterson decrement (Davidsen, Kriss, & Zeng 1996). The initial gas temperature was assumed to take the value for which photoionization heating balances the cooling due to collisional processes and Compton scattering. For simplicity, we take the gas to be homogeneously contaminated by metals (C, Si, N, O) with solar relative abundances and an absolute metallicity of 10^{-2} solar. Effects of time-dependent and/or inhomogeneous chemical enrichment were neglected. Later, we shall consider different total and relative metallicities and briefly discuss implications of an inhomogeneous metal contamination.

2.3. The Matter and Temperature Distribution

Some of the simulations were run up to the present epoch. For an individual set of initial conditions, typically between one and three disklike galaxies with circular velocities between 80 and 200 km s⁻¹ have formed by now. Each consists of several thousand particles. In addition, a couple of halos with smaller masses and circular velocities (about 50 km s⁻¹) are present. Size, mass, and circular velocities of these disks are in good agreement with observed spiral galaxies. Compared to present-day spiral galaxies, however, the disks are too concentrated. This may be an artifact due to the neglect of energy and momentum input by star formation and active galactic nuclei.

Tracing the evolution of the dark matter halo of a present-day galaxy backward in time, one finds that at $z = 3$ it has “split” into several progenitors separated by several hundred kpc. While the circular velocities of these progenitors are generally slightly smaller than that of the galaxy which they will later form, this is not true for the most massive progenitors. These have the same or even higher circular velocities even at redshifts of 3 to 5, although their mass might be a factor 10 smaller (White & Frenk 1991; Steinmetz 1996a). The progenitors probably suffer from the same overcooling problem as their present-day counterparts. This will have small effects for intermediate column density absorbers, but conclusions regarding damped Ly α absorbers should be drawn with some caution.

Figure 1 shows the column density and temperature distribution (H I weighted along the LOS) at $z = 3.07$ (bright = high column density/hot) of a typical simulation box in which three galaxies with circular velocity $v_c \sim 100$ km s⁻¹ have formed at $z = 0$. The area shown is 700 kpc across (proper length). Individual PGCs are embedded in a filamentary network. Regions leading to a single $v_c \sim 200$ km s⁻¹ galaxy look similar, with individual components scattered over several hundred kpc.

The temperature in the gas rises from less than 10^4 K at the center of expansion-cooled voids (large diffuse dark areas) to a few times 10^4 K for the gas in the filaments. Higher temperatures up to several 10^5 K occur in spheroidal envelopes within ~ 30 kpc of the PGCs. These envelopes of hot gas arise when infalling gas is shock heated to temperatures of the order of the virial temperature, but the density of this gas is low enough that cooling times are

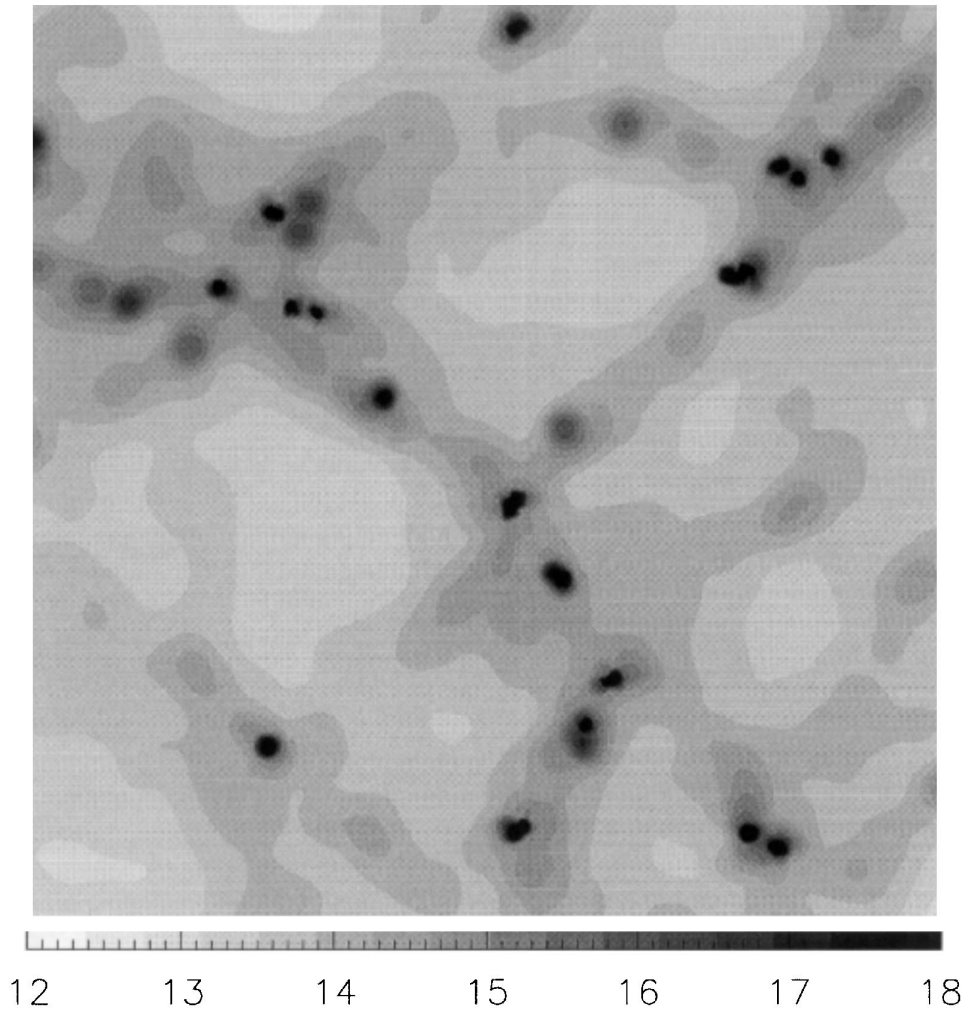


FIG. 1a

FIG. 1.—Fig. 1a shows a gray-scale plot of the projected H I column density ($\log N$) of the inner 700 kpc of a simulation box at $z = 3.07$ that will contain three $v_c \sim 100 \text{ km s}^{-1}$ galaxies at $z = 0$. Fig. 1b shows the temperature ($\log T$, H I column density weighted) for the same box.

long compared to dynamical timescales. The temperature, the location, and the mass fraction of this hot gas component can depend sensitively on the assumed spectral shape of the UV background and on the metal enrichment (Navarro & Steinmetz 1997). In the innermost few kpc of the PGCs, the cooling timescales are always short compared to the dynamical timescale, and the dense gas cools precipitously to temperatures below 10^4 K.

2.4. The Ionization State of the Gas

We have used the photoionization code CLOUDY (Ferland 1993) to calculate the ionization state of the gas for the temperature, density, and UV background of each SPH particle in the simulation. (Self-)shielding from UV radiation in optically thick regions was generally not taken into account. Thus, quantitative results for LOS with column density above 10^{17} cm^{-2} need to be viewed with some caution. Below we will concentrate on the ionic species H I, C II, C IV, Si IV, N V, and O VI, which are expected to provide some of the strongest observable lines in low and intermediate column density absorbers. As discussed in Papers I and II, observations and SPH simulations indicate that gas

temperatures can significantly deviate from the equilibrium value where photoheating balances line cooling processes. It is then important to use the actual gas temperature to calculate the ionization state of the different states. Figure 2 shows the ratios of various metal to H I column densities as a function of density for our chosen ionic species and a set of temperatures between 10^4 and 10^6 K. At high and intermediate densities, the metal column density is generally increased relative to the H I column density with increasing temperature, while at small densities, the opposite is true. Si IV and C IV are especially temperature sensitive in the temperature and density range most relevant for intermediate column density absorption systems around $n_{\text{H}} \sim 10^{-4} \text{ cm}^{-3}$ and $T \sim 5 \times 10^4$ K.

Figure 3 shows logarithmic column density contours for all six ions in steps of 1 dex. C II and Si IV are confined to dense regions marking likely sites of star formation in the center of the PGCs. C IV traces the hotter filaments and halos, while O VI matches well the low column density H I contours and traces low-density gas of any temperature (see Chaffee et al. 1985, 1986). In the box shown, the covering factor for detectable hydrogen absorption is 100%. The

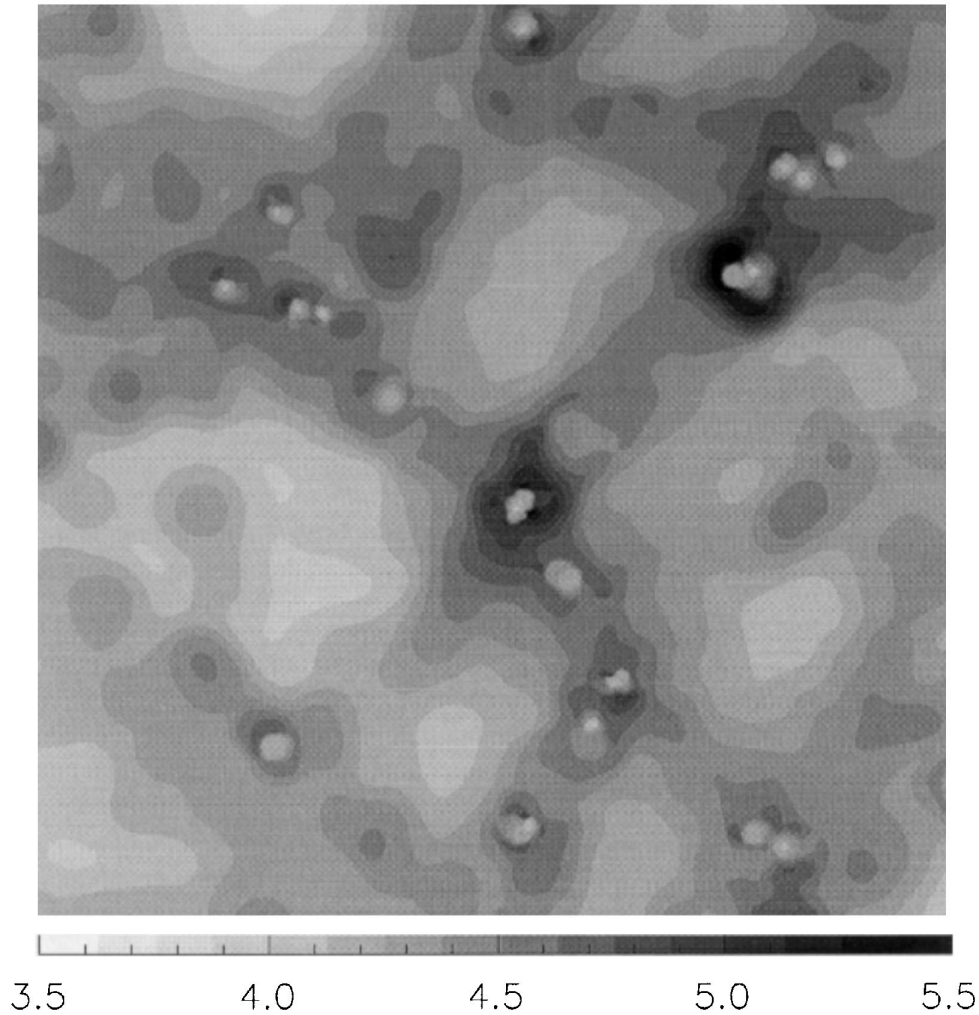


FIG. 1b

same is true for O VI if the metal contamination is indeed homogeneous and does not drop in regions outside the filamentary structure. Approximately one-third of all LOS give detectable C IV absorption.

2.5. Generating Artificial QSO Spectra

To analyze the appearance of the galaxy-forming region in absorption, we drew 1000 LOS and generated artificial spectra for the simulation box shown in Figure 1 (see § 2.3). The LOS had random orientations and random offsets within ± 225 kpc from the center of the box. Optical depth $\tau(v)$ profiles along the LOS were constructed projecting the Voigt absorption-line profile caused by the column density of each individual spatial pixel onto its proper position in velocity space, using the relation (for the H I Ly α line)

$$\tau(v) = \sum_i \tau_i(v - v_i) = 1.34 \times 10^{-12} \frac{dN}{dv}(v) \quad (1)$$

(see Gunn & Peterson 1965). Here $\tau_i(v - v_i)$ is the optical depth of the Voigt profile at the observed velocity v , caused by the column density ΔN_i in spatial pixel i , moving with velocity $v_i = v_{\text{pec}}(i) + v_{\text{Hubble}}(i)$. This can be expressed in

terms of the column density per unit velocity, dN/dv at v . Units of N are cm^{-2} , and v is in km s^{-1} .

The spectra were made to resemble typical Keck data obtainable within a few hours from a 16th–17th mag QSO (signal-to-noise ratio = 50 per 0.043 \AA pixel, FWHM = 8 km s^{-1}). These “data” were then treated and analyzed in exactly the same way (by fitting Voigt profiles) as actual observations. An absorption line was deemed detectable when the equivalent width had a probability of less than 10^{-5} (corresponding to a greater than 4.75σ event) to have been caused by a statistical fluctuation.

3. ABSORPTION-LINE FORMATION IN REGIONS OF ONGOING GRAVITATIONAL COLLAPSE

Having access to the three-dimensional gas/temperature distribution and the velocity field of the gas, we are able to study the line formation process as a function of the characteristic physical properties of the absorbing structures. We expect the general mechanisms to be similar to those found earlier for H I absorption features (Cen et al. 1994; Zhang et al. 1995; Hernquist et al. 1996; Miralda-Escudé et al. 1996). The emphasis of the present work is, however, on the much

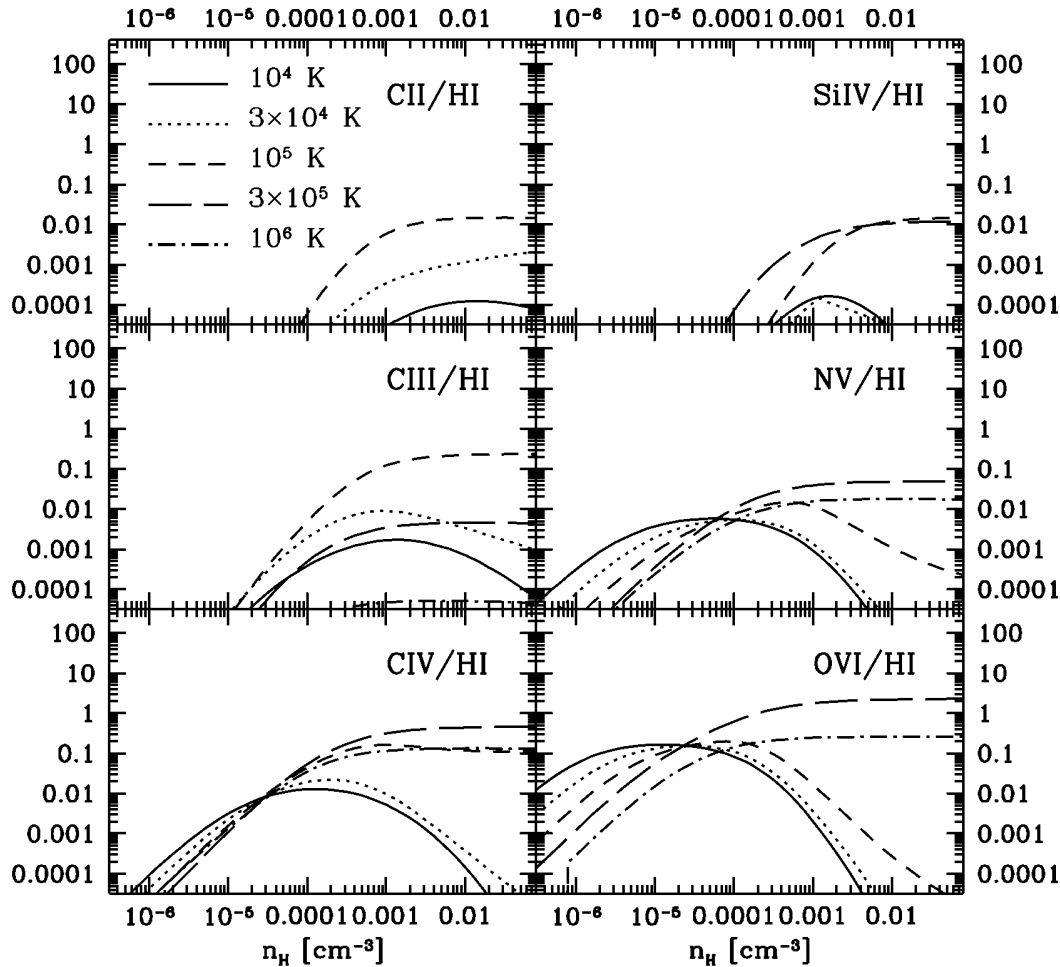


FIG. 2.—Column density ratios relative to H I for six different ionic species calculated with CLOUDY for fixed density and fixed temperatures between 10^4 and 10^6 K as indicated on the plot. A power law with $\alpha = -1.5$ and $J_{-22} = 3$ was assumed for the background UV field.

narrower absorption lines from metal ions. Smaller Doppler parameters and lower column densities of the heavy element lines enable us to study the velocity structure in galactic potential wells, where the corresponding H I Ly α lines are saturated and strongly blended. The resolution of the present simulations is higher than that of previous work, so we can pursue the physical quantities into regions of larger densities and can study the fate of objects of small mass.

3.1. Environments Causing Specific Absorption Patterns

The following figures illustrate a few “typical” situations in which gravitational collapse gives rise to C IV and other metal absorption features. The panels give (top to bottom) the spectra of the six ions offset vertically by 0.5, the total baryon density, the temperature, and the peculiar velocity. The x-axis is the spatial coordinate along the LOS labeled by the relative velocity each position would have if following an undisturbed Hubble flow. As the structures have different sizes in position space and redshift space, we decided to plot a spectral region larger than the spatial size of the box to show the fullest extent of the absorption system in velocity space. Making this particular choice creates the impression of a lack of absorption both blueward and redward of the center as any absorption features created beyond the spatial boundaries of the simulated

region but projected into the velocity space shown are not present.

In the case of C IV, Si IV, N V, and O VI, only the stronger transition of each doublet is shown. The dotted lines connect the spatial positions of overdense regions (selected manually) to their density weighted positions in velocity space.

3.1.1. Collapsing Regions of Moderate Overdensity

Figure 4a shows a LOS producing an intermediate column density H I profile. The line is saturated but not yet damped. In LOS passing very closely to at least one PGC, generally a single sharp density peak dominates the absorption line formation (see the following figures), but more often the LOS passes through regions of smaller overdensities just about to collapse into a single object. The peculiar velocity field displays a typical infall pattern (redshift with respect to the Hubble flow for gas falling in from the front, blueshift for gas falling in from behind, a jump at the location of the density maximum). C IV and O VI are the only metals that can be detected. The absorption features are similar in appearance to the “partial Ly α limit systems” studied by Cowie et al. (1995). In this particular case, the individual density peaks have converged in velocity space to form a caustic (see McGill 1990), but the enhanced density in physical space is still much more

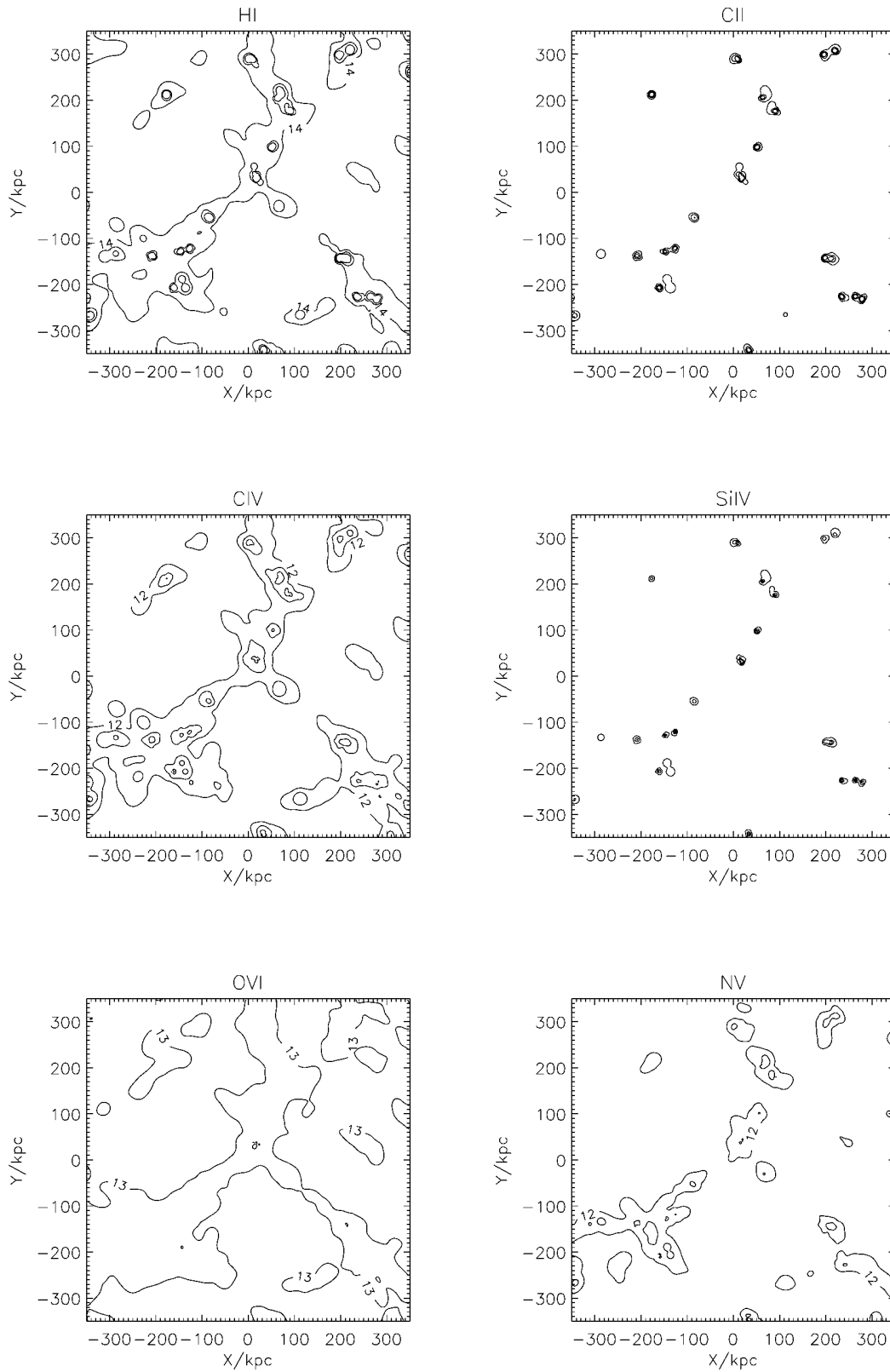


FIG. 3.—Projected column density of the inner 700 kpc of a simulation box at $z = 3.07$ that will contain three $v_c \sim 100 \text{ km s}^{-1}$ galaxies at $z = 0$. Shown are logarithmic column density contours in steps of 1 dex for H I, C II, C IV, Si IV, N V and O VI.

important for producing the absorption line (see also Miralda-Escudé et al. 1996). In principle, velocity caustics may reduce the contribution of the Hubble expansion to the total velocity width of absorption lines. We find, however,

that this rarely occurs. In most cases, infall velocities overcompensate the Hubble flow. The ordering of two absorption lines in velocity space can even be reversed relative to their spatial positions.

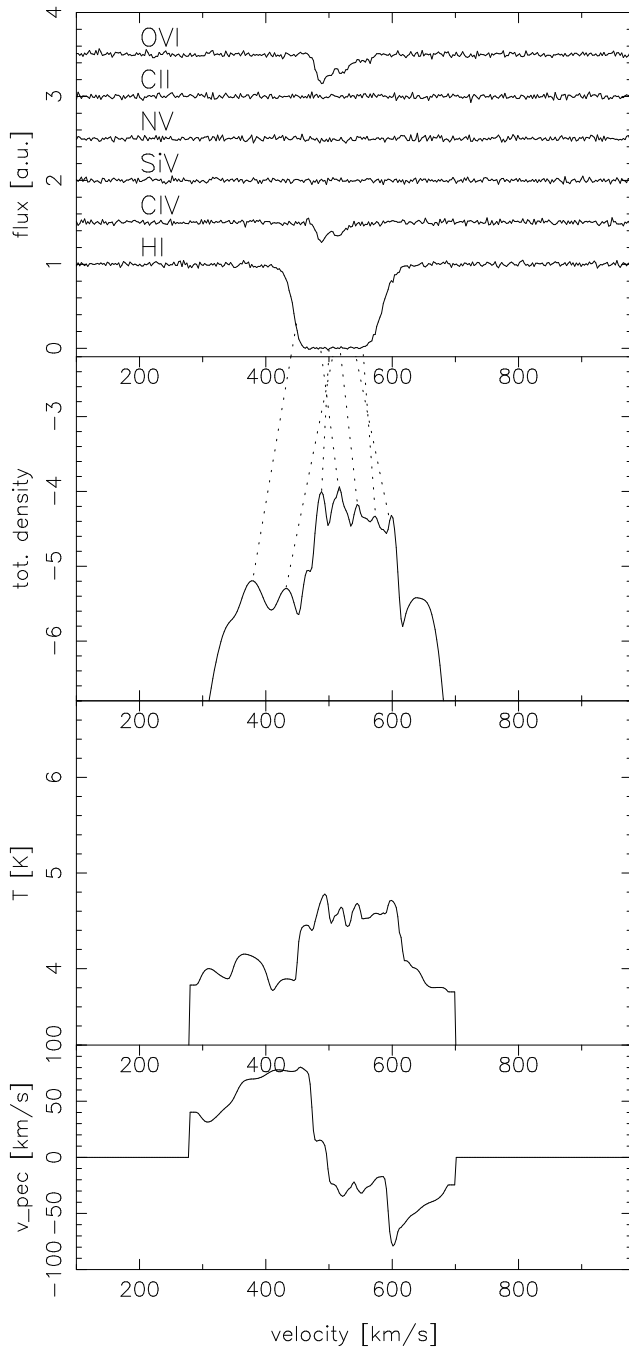


FIG. 4a

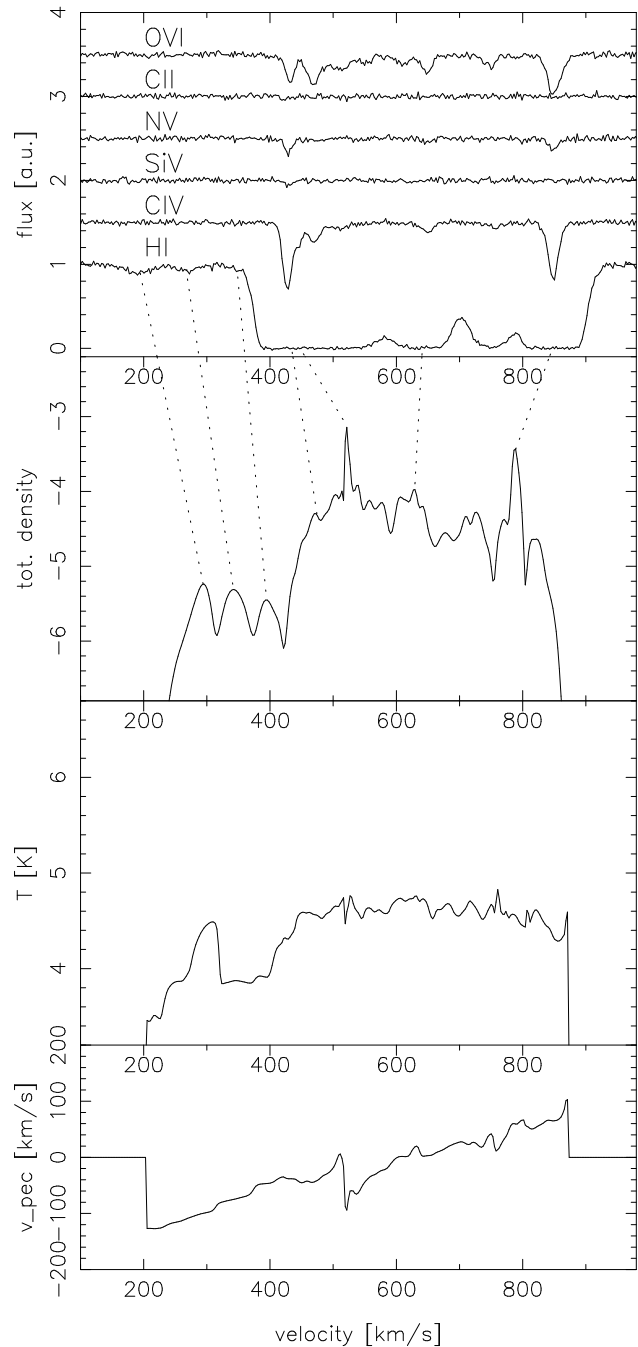


FIG. 4b

FIG. 4.—(a): Spectrum of a LOS through a collapsing region of moderate overdensity producing intermediate column density H I and weak C IV and O VI absorption. (b): LOS along a filament apparently expanding faster than the Hubble flow. The panels give (top to bottom) the spectra of the six ions offset vertically by 0.5, the total baryon density, the temperature, and the peculiar velocity (see § 3.1). In the case of C IV, Si IV, N V, and O VI, only the stronger component of each doublet is shown.

3.1.2. Large Velocity Spread and Chance Alignments with Filaments

Absorption caused by a chance alignment between the LOS and a filamentary structure is seen in Figure 4b. The filaments generally lie at the boundaries of underdense regions (“voids”) and appear to expand with velocities in excess of the Hubble flow. This is apparent from the divergent dotted lines and the ramplike increase of the peculiar velocity as a function of real-space distance. Such structures, rather than deep potential wells, are likely to be

responsible for the largest observed velocity splittings of C IV systems, whereas moderate velocity splittings (up to $200\text{--}300\text{ km s}^{-1}$) are often due to a complex temperature distribution or ionization structure internal to individual PGCs (see also Paper I).

3.1.3. “Damped Ly α Systems”

Figure 5 shows two “damped Ly α systems.” Currently we are limited to qualitative statements about the spatial extent and ionization state of damped Ly α systems as

neither self-shielding nor energy/momentum input by star formation or AGNs have been taken into account. Nevertheless, in agreement with Katz et al. (1996), we find that for small impact parameters, column densities become large enough to produce damped Ly α absorption lines. Damped systems are usually dominated by one large density maximum. The density peak corresponds to a local temperature minimum owing to cooling of the dense gas at the center and is surrounded by a shell of hotter infalling shock-heated gas. This leads to the characteristic double-hump structure in the temperature diagram of Figure 5a. The absorption lines for the various ions of the system shown in

Figure 5a appear rather similar to each other in terms of position and line shape, with the exception of O VI, which arises at much larger radii. In general, the maxima of the high-ionization species for these highly optically thick systems need not coincide with the centers of the H I lines and those of lower ionization species. Figure 5b illustrates a situation where the component structure has a very complex origin. While the strongest C II and Si IV components coincide with the center of the damped Ly α line, the C IV and N V positions are far off, which indicates differential motion between the high and low ionization regions.

It is likely that the effects of hydrodynamic and thermal

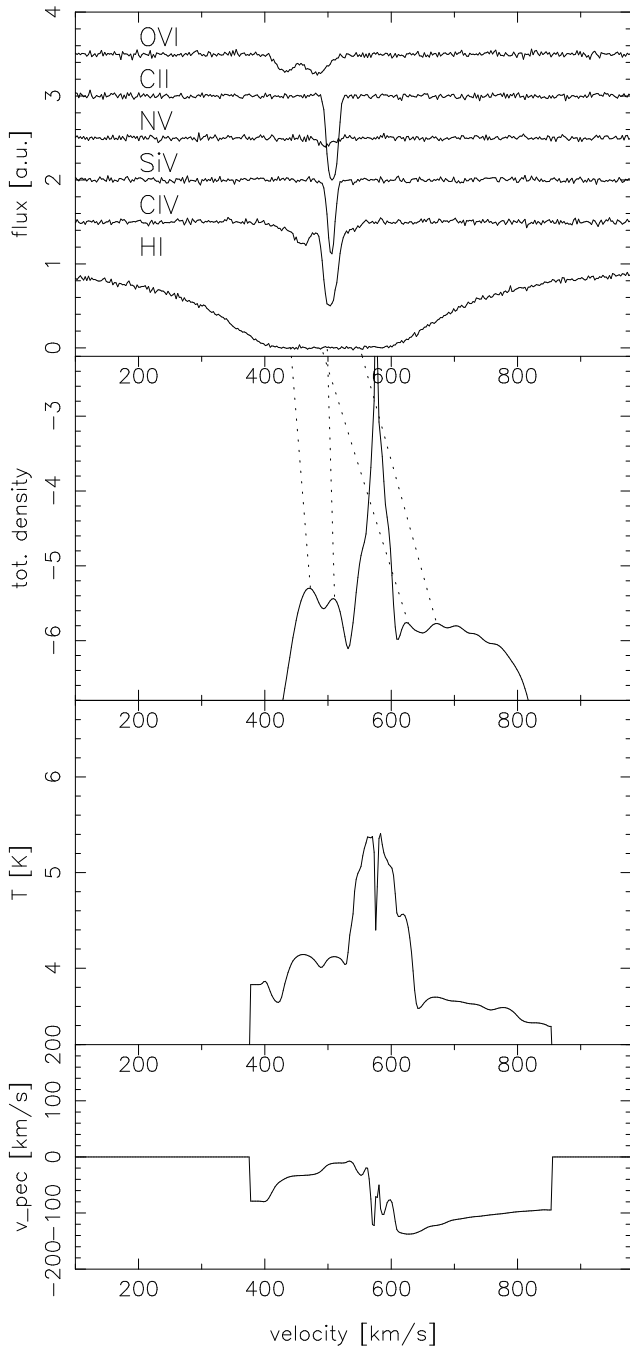


FIG. 5a

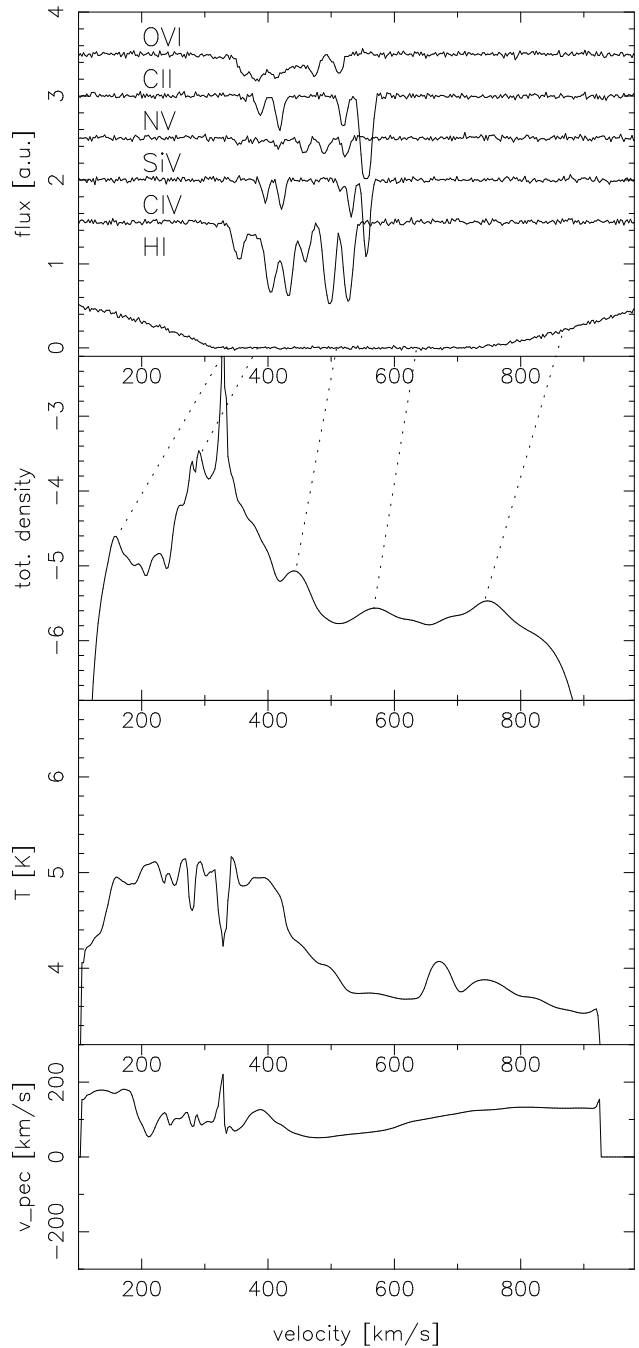


FIG. 5b

FIG. 5.—Damped Ly α systems

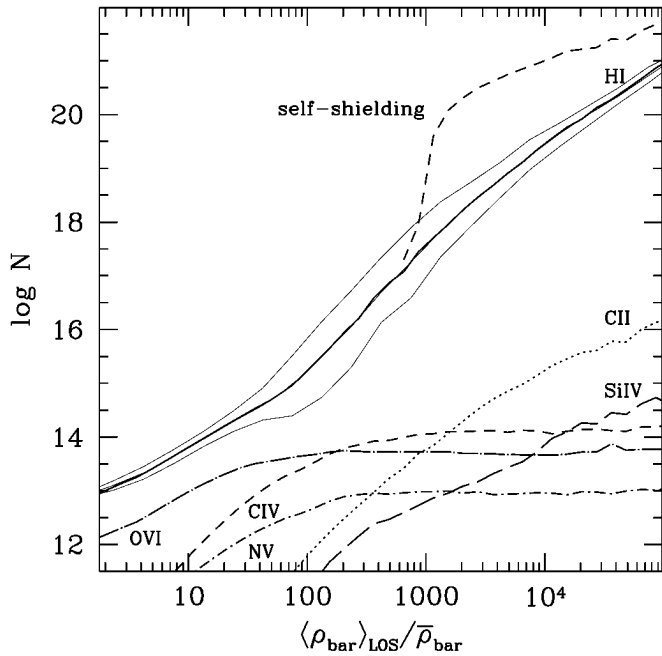


FIG. 6.—Mean (of the log) of the projected column density as a function of overdensity $\langle \rho_{\text{bar}} \rangle_{\text{LOS}} / \bar{\rho}_{\text{bar}}$ (column density-weighted along the line of sight) for the simulation box shown in Fig. 1. For H I, the thin solid lines show the $\pm 1 \sigma$ range in column density at fixed overdensity.

instabilities and star formation will lead to substantial additional density and temperature variations on scales of kpc or less, not captured by the present simulation. We do not know how much of this structure would actually be visible in absorption, but the number of discernible absorption components seen in the simulated spectra is probably best interpreted as a lower limit to the number of components in actual data.

3.2. The Absorption Properties of Individual Protogalactic Clumps

The solid curves in Figure 6 show the good correlation between the mean $\log N(\text{H I})$ and the baryonic overdensity in a typical simulation box. Also shown is the mean $\log N$ for our canonical set of ionic species. As expected, the strength relative to H I varies considerably from species to species. C II and Si IV are strong at high H I column densities/baryonic overdensities, while C IV dominates at intermediate column densities and O VI probes the low-density regime. We have also plotted a simple self-shielding correction for large H I column densities. The correction was calculated with CLOUDY specifying the total column density and mean density along the LOS.

Figure 7 shows how the spectral features change with distance from a fully collapsed clump. The plot consists of a mosaic of LOS separated by 3 kpc from each other in the x - and y -directions on the sky. The center of the clump is close to the top right-hand corner. The H I Ly α line exhibits damping wings within the central ≈ 6 kpc.

To quantify the spatial coherence of the absorption properties in more detail, we have investigated a set of random LOS close to a typical PGC ($M \approx 1.2 \times 10^9 M_{\odot}$) in the simulation. Figure 8 shows the column densities as a function of impact parameter for a set of randomly oriented LOS. A sharp drop from $\log N(\text{H I}) \geq 20$ to $\log N(\text{H I}) \approx 15$

occurs within the first 5–10 kpc. At H I column densities above $\log N \geq 17$, self-shielding should become important. This will lead to an even steeper rise toward smaller radii. After the rapid drop, the H I column density decreases very gradually, still exceeding $\log N(\text{H I}) \approx 14$ at 100 kpc. The typical size of the damped region of a protogalactic clump in our simulation taking self-shielding into account should be about 5 kpc. However, as pointed out previously, this value might increase, once feedback processes are taken into account.

Currently a 10 m telescope can detect H I column densities of order 10^{12} cm^{-2} , which means that the detectable H I radius extends far beyond 100 kpc. The largest detectable metal absorption cross section is subtended by C IV and probably O VI (bottom panel on the right); at a detection threshold of $N(\text{C IV}) \sim 10^{12} \text{ cm}^{-2}$ (realistic for very high signal-to-noise ratio data), the radius is ~ 30 kpc; Si IV at the same significance level (taking the larger oscillator strength into account) would be detectable out to about 12 kpc. The decrease of the higher ions C IV and N V at the lowest radii is due to the increase in density; it should be even more pronounced if radiation transfer were implemented. Figure 9 gives the ratios of the LOS integrated column densities for several ions. In particular, the second panel on the left shows once more the importance of the O VI ion, which should be detectable at the largest radii with similar or even higher significance than the C IV lines. Thus, in spite of the difficulty of observing O VI in the Ly α forest, the O VI/C IV column density ratio should be the best measure of the impact parameter.

4. OBSERVATIONAL TESTS

4.1. Column Density Distributions as a Test of the Gas Distribution and Metallicities

Before discussing the overall column density distribution of H I and the metal ionic species in our simulations, we stress again that our simulation boxes were not chosen randomly (see § 2.2). At our redshift of interest ($z = 3$), the mean baryonic density of the simulation boxes containing low (high) circular velocities halos is a factor 1.27 (2.97) larger than the assumed mean baryonic density of the universe for the inner 700 (proper) kpc cube. Furthermore, H I column densities projected across the simulation box are generally larger than a few times 10^{13} cm^{-2} . Below we will concentrate on properties of the four boxes containing low circular velocities halos at $z = 3.1$ for which the overdensity is moderate and which should be closest to a fair sample.

Column density distributions/ratios of ionic species with different ionization potentials are an important diagnostic of the ionization parameter, the spectral shape of the ionization field, the relative element abundances, and the temperature of the gas (see, e.g., Bergeron & Stasinska 1986; Chaffee et al. 1986; Bechtold, Green, & York 1987; Donahue & Shull 1991; Steidel 1990; Viegas & Gruenwald 1991; Ferland 1993; Savaglio et al. 1996; Songaila & Cowie 1996). In our case, the distributions of densities and temperatures are predicted by the simulation (only weakly dependent on the input radiation field), so the remaining adjustable parameters are the elemental abundances and the properties of the ionizing radiation.

4.1.1. Column Density Distribution Functions

We define the differential column density distribution as

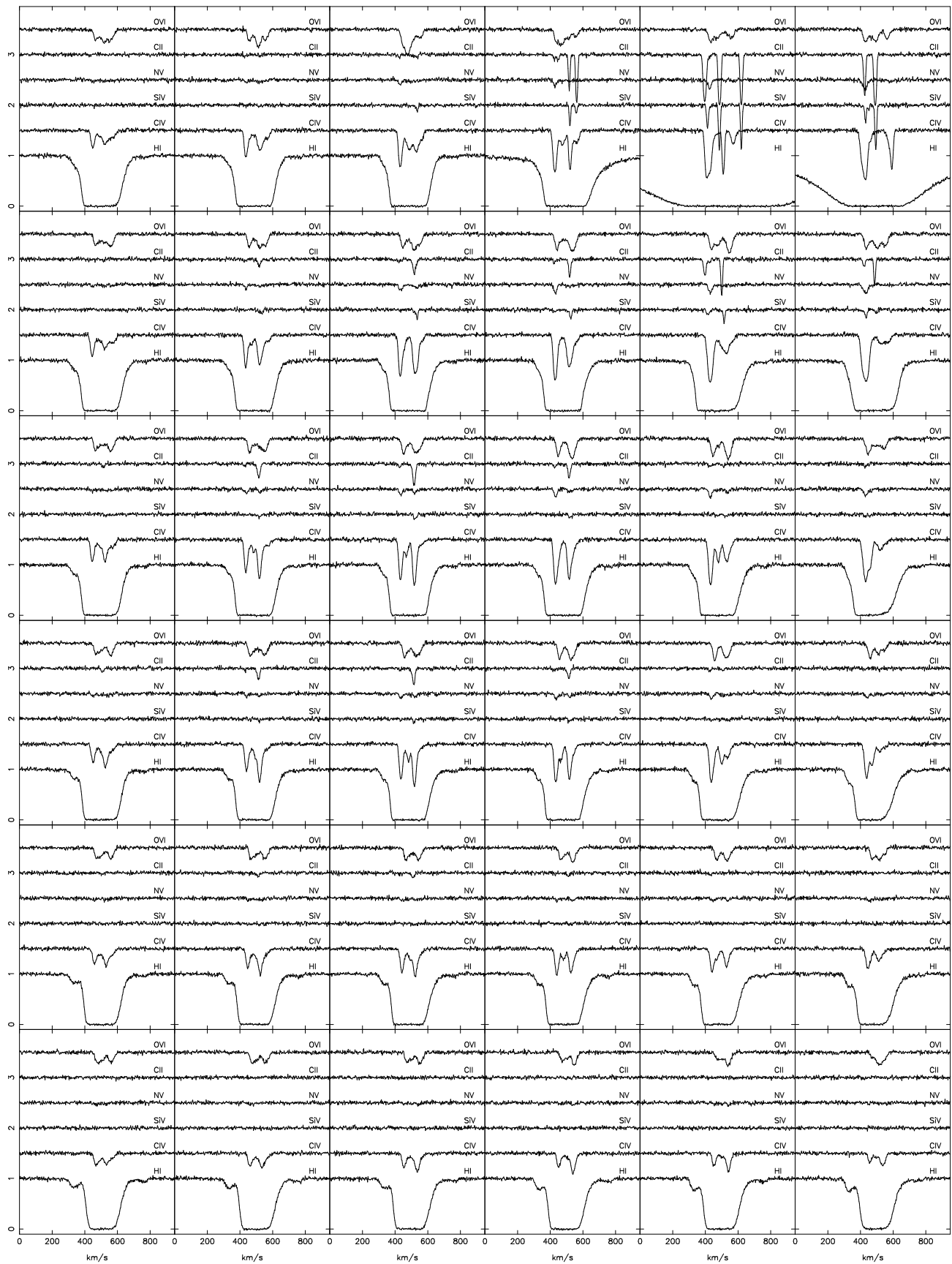


FIG. 7.—Mosaic of 6×6 lines of sight near a collapsed clump, separated by 3 kpc in each direction on the sky. The center of the collapsed object is close to the top right-hand corner. The panels give the spectra of the six ions offset vertically by 0.5 for clarity. In the case of C IV, Si IV, N V, and O VI, only the stronger line of each doublet is shown.

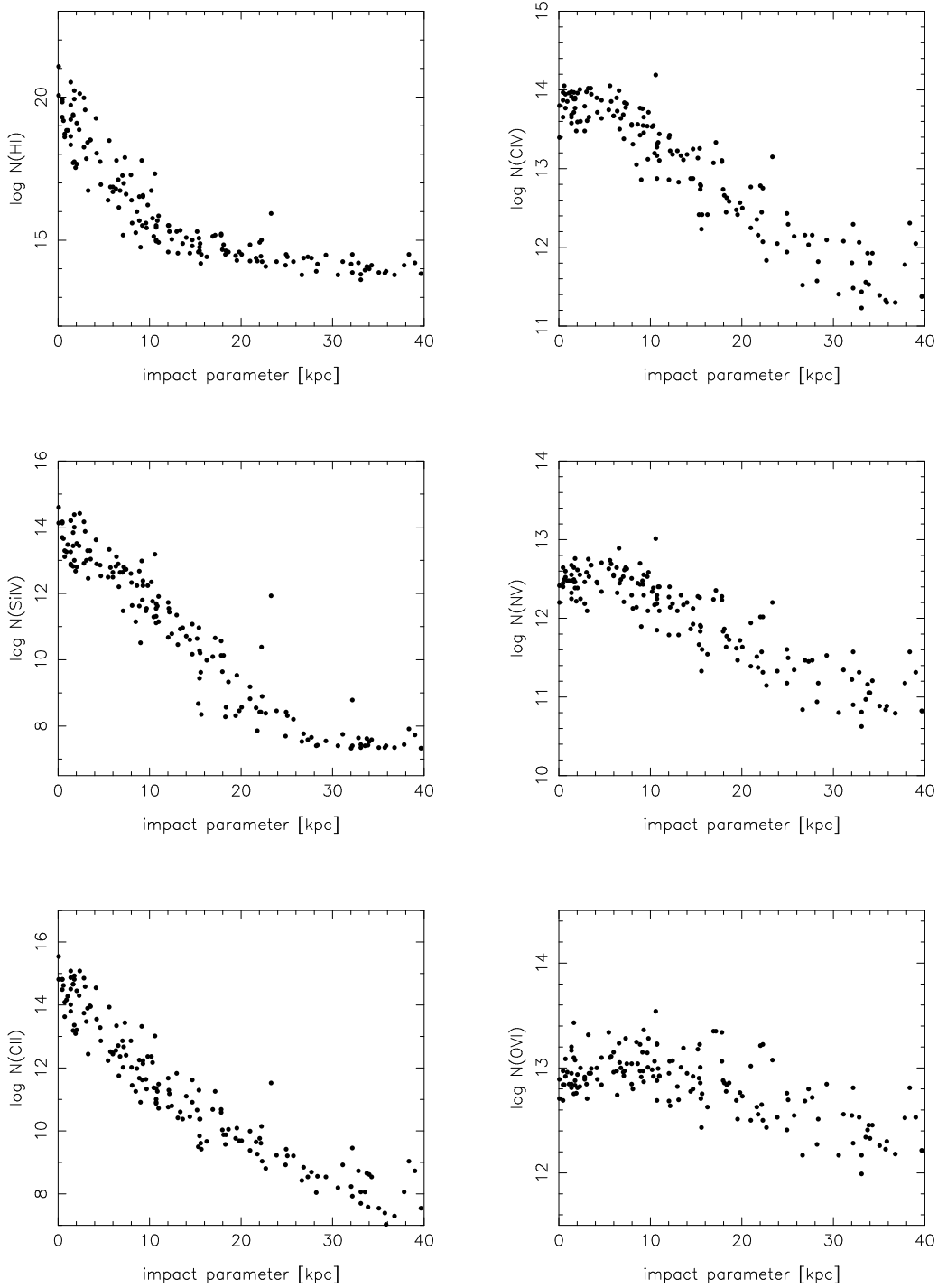


FIG. 8.—Integrated column densities along random lines of sight for the six ions as a function of impact parameter from the center of a protogalactic clump with $1.2 \times 10^9 M_{\odot}$.

usual

$$f(N) = \frac{d^2 \mathcal{N}}{dX dN}, \quad (2)$$

where \mathcal{N} is the number of lines and $dX = (1+z)^{1/2} dz$ (for $q_0 = 0.5$). The curves in Figure 10 give $f(N)N$ at $z = 3.07$ for the four simulation boxes shifted in column density by $+0.3$ dex, whereas the crosses show the observed distribution (Petitjean et al. 1993). The data on the metal ions are again

for a constant metallicity of $[Z/H] = -2$. The self-shielding correction for large H I column densities mentioned in § 3.2 is also shown. The shape of the observed distribution is matched reasonably well by the simulations once the self-shielding correction is applied. As pointed out, e.g., by Hernquist et al. (1996) and Miralda-Escudé et al. (1996), the H I column density should scale with the baryon fraction, the strength of the ionizing background, and the Hubble constant as $\Omega_b^2 h^3 / J$. In Figure 10, we got a reasonably good

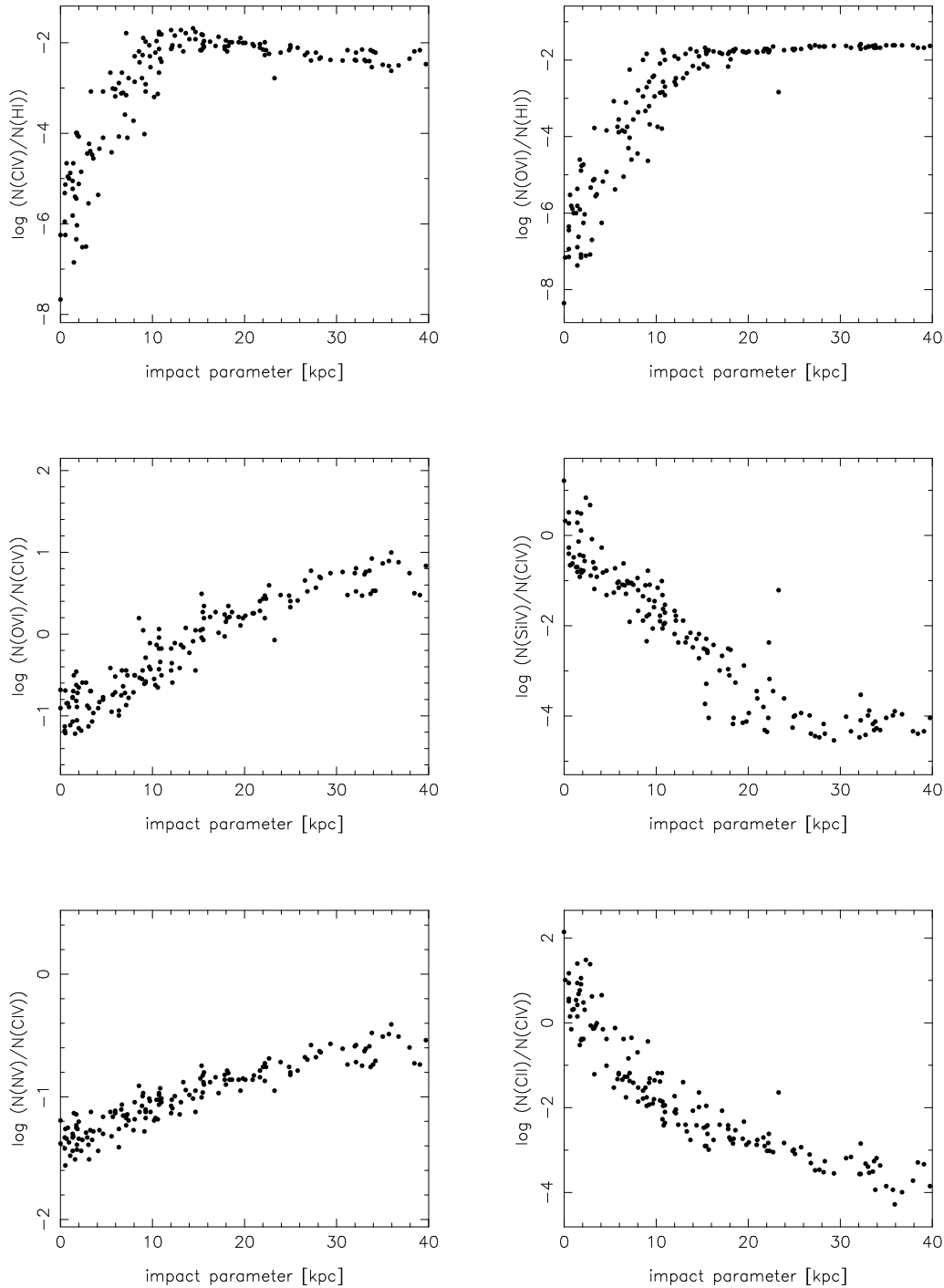


FIG. 9.—Ratios of the integrated column density along random lines of sight for several ions as a function of impact parameter from the center of a protogalactic clump with $1.2 \times 10^9 M_{\odot}$.

fit for the H I column density distribution by applying a shift of +0.3 dex to the H I column density. The same shift was also applied to the metal column densities even though one should note that these depend on Ω_b and J in a more complicated way so that this might not be completely appropriate. Our “best fit” corresponds to $[\Omega_b/(0.05 h_{50}^{-2})]^2/(J_{-22} h_{50}) \approx 0.7$, similar to but slightly lower than the value found by Hernquist et al. (1996). Taking into account that the mean baryonic density of the volume used to calculate the column density distribution is a factor 1.27

larger than the assumed overall mean baryonic density should increase this value improving the agreement further. We do also find a deficit of systems with H I column densities around 10^{17} cm^{-2} , but it is smaller than the discrepancy by a factor 10 reported by Katz et al. (1996).

4.1.2. Column Density Ratios for Random Lines of Sight

Figure 11 shows column density ratios for various ions, integrated along randomly offset and oriented LOS through the box described at the end of § 2.3. The most

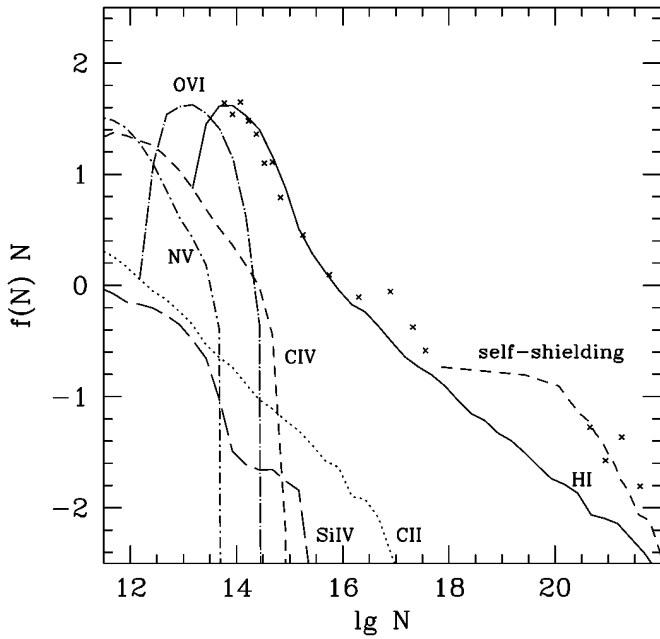


FIG. 10.—Column density distribution [$f(N) N$] at $z = 3$ for six different species in the simulation. Crosses show the observed column density distribution (Petitjean et al. 1993). The column density normalization is described in § 4.1.

readily observable ratio is C IV/H I, which in the simulations has a maximum of about -2.2 at $N(\text{H I}) = 10^{15} \text{ cm}^{-2}$ in the log. This is consistent with the range of values measured by Cowie et al. (1995), but a better match can be found with a carbon abundance of $[\text{C}/\text{H}] = -2.5$ instead of the originally adopted $[\text{C}/\text{H}] = -2$. At higher column densities, C IV recombines to form C III and C II with increasing density and shielding. At lower column densities, C IV/H I also declines as carbon becomes more highly ionized into C V. This effect will cause difficulties for searches for carbon enrichment in the Ly α forest at column densities much lower than the presently accessible limits in H I (10^{14} cm^{-2}), as not only the H I column but also the C IV/H I ratio declines.

Results obtained from Voigt profile fitting a subset of the spectra (using the software package VPFIT; Carswell et al. 1987) are shown in Figure 12. Solid dots are measurements from the simulation. For comparison, open boxes give observational data for C II, C IV, Si IV, and N V by Songaila & Cowie (1996) and for O VI from Rauch et al. (1997). The circles show observational upper limits or (for O VI) indicate undetermined column densities in cases of severe blending with Ly α forest lines. The thin diagonal lines indicate the approximate detection limits for absorption features in the simulated spectra. Most of the general trends in the observed column density ratios are well reproduced. The scatter in the column density ratios between different metal ionic species is similar to that found observationally. Obviously the simulations produce a realistic range of ionization conditions.

There are, however, some interesting discrepancies between simulated and actual data. First, we note that the scatter in C IV/H I (*top left-hand panel*) for the observations is much larger than that in the simulations (where constant metallicity was assumed). We take this to imply that the

carbon fraction and perhaps also the absolute metallicity in the outskirts of protogalactic objects at $z \sim 3$ fluctuate over 1–2 orders of magnitude throughout the column density range $N(\text{H I}) 10^{14}$ to 10^{18} cm^{-2} . It is interesting to note that a similar scatter is seen in $[\text{C}/\text{Fe}]$ in metal-poor stars (McWilliam et al. 1995; Timmes, Woosley, & Weaver 1995).

There are also some obvious differences between the absolute levels of the observed and simulated mean column density ratios. While the abundance ratios for the high-ionization species (C IV, N V, and O VI) in the simulation agree reasonably well with the observations, Si IV and C II are significantly off, with the simulated Si IV/C IV and C II/C IV ratios lower by a factor 10 than the observed values.

4.1.3. Matching the Observed Column Density Ratios

Some of these discrepancies can be reduced by an appropriate modification of the relative abundances. So far, we have assumed *solar relative abundances*. The generally low abundances in present-day Galactic halo stars (which may contain a fossil record of the high- z gas abundances) as well as optically thin C IV systems (Cowie et al. 1995) and high-redshift damped Ly α systems (Pettini et al. 1994; Lu et al. 1996) indicate that relative metal abundances like those in very metal poor stars (McWilliam et al. 1995) may be more appropriate. Below we will discuss the effect of changing the abundance pattern from solar values to $[\text{C}] = [\text{N}] = 0$; $[\text{Si}] = [\text{O}] = 0.4$. The brackets denote the difference to solar abundances in dex.

Some improvement may also be expected from a different intensity or spectral shape of the ionizing radiation background. Figure 13 shows the influence of such changes on various column density ratios. The solid curve shows the values for the $\alpha = 1.5$ power-law spectrum. The other curves are for several different spectral shapes and normalizations of the UV background: a power law with intensity increased and decreased by factors of 3; a spectrum taking intergalactic absorption and emission into account (Haardt & Madau 1996); and a power law with a step-shaped break at 4 ryd (flux reduced by a factor 100 at 4 ryd, constant flux for higher energies up to the point where the flux equals that of the underlying power law). The effect of the absorption edges in the Haardt & Madau spectrum on the ion ratios considered here is generally small for the relevant column densities. A power law with slope 1.5 gives a good approximation. Changing the normalization has noticeable but moderate effects on the Si IV/C IV and C II/C IV ratios. Otherwise, the changes are again small. The case of a power law with a 4 ryd cutoff, however, leads to strong departures in the ion/H I and in the ion/ion ratios for a given H I column density. A spectrum of the last kind was suggested by Songaila & Cowie (1996) and Savaglio et al. (1996) to account for large observed Si IV/C IV ratios at $z > 3$. These authors consider an increasing He II opacity or an increasing stellar contribution to the UV background toward higher redshifts as possible causes for a softer spectrum.

However, for a fixed C IV column density, the power law with 4 ryd cutoff actually even lowers the Si IV/C IV and C II/C IV ratios relative to those obtained with the originally adopted $\alpha = 1.5$ power law. Moreover, such a spectrum would imply a factor 3–10 smaller carbon abundance. Apparently, changing the UV radiation field does not dramatically improve the overall agreement with the observed ion ratios.

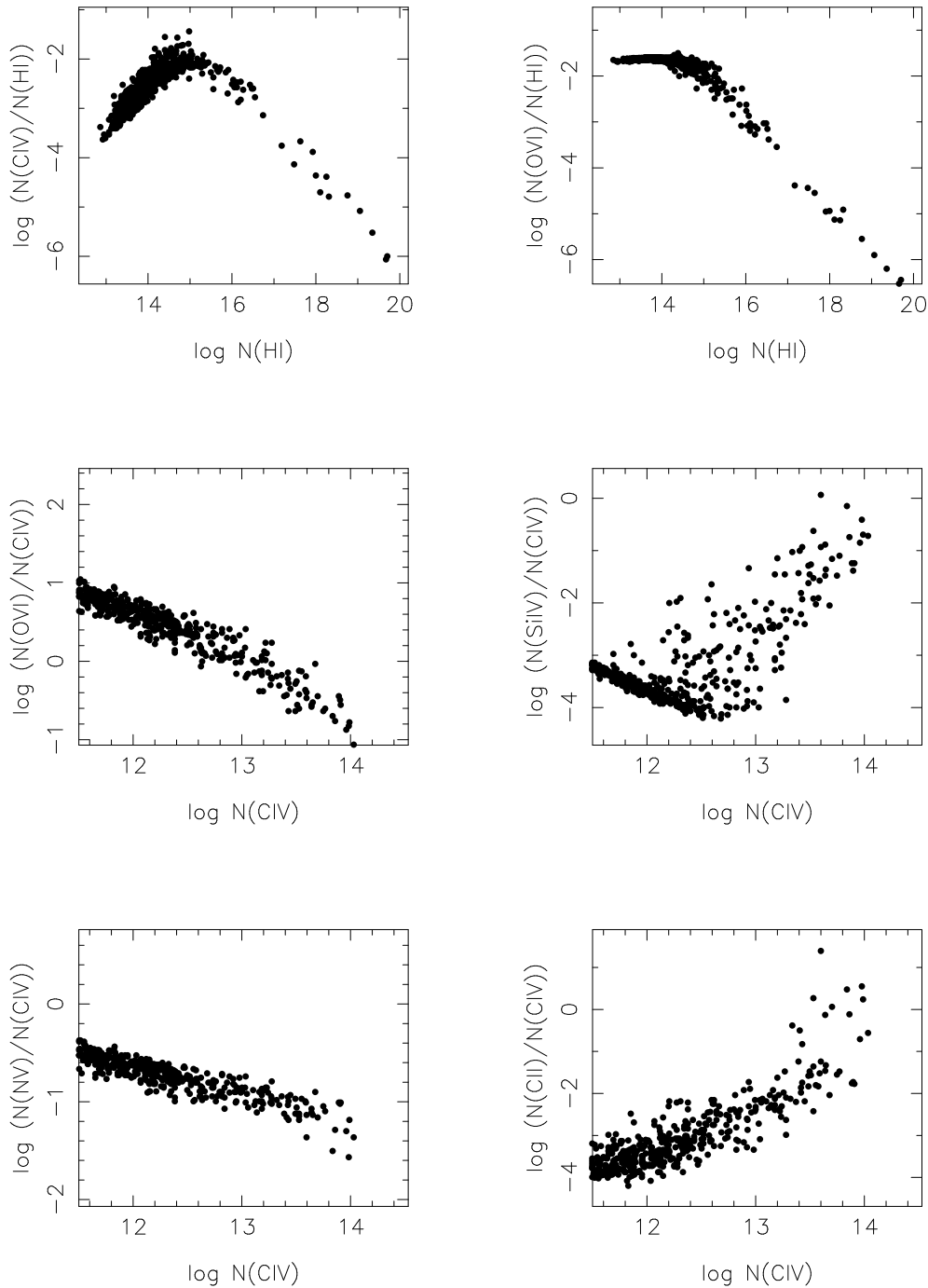


FIG. 11.—Ratios of the integrated column densities along random lines of sight for several ionic species as a function of H I or C IV column density

The observed and simulated column density ratios are compared in Figure 14, after adopting some of the changes discussed above (metallicity reduced by 0.5 dex to $[Z/H] = -2.5$; metal-poor abundance pattern; spectrum as suggested by Haardt & Madau). The discrepancy for Si IV and C II has now been significantly reduced: the contribution to the shift in the Si IV/C IV versus C IV came in equal parts from the adjustment in relative and absolute metallicity, whereas the C II/C IV versus C IV ratio improved mostly because of the decrease in absolute metallicity. Thus the agreement is now quite good for Si IV, C II, and C IV. O VI and N V are slightly further off but—given the large

observational uncertainties in these two ions—probably consistent with the data.

4.2. The Doppler Parameter as Indicator of Gas Temperatures and Small-Scale Bulk Motions

Temperature and bulk velocity measurements from individual absorption lines are useful discriminants for the environment of heavy element absorption systems. The actually observable quantity is the Doppler parameter b ($=2^{1/2}\sigma$) of the absorbing line. The line width results from a convolution of the thermal motion and the small scale bulk motion. Measurements of the Doppler parameter for ionic

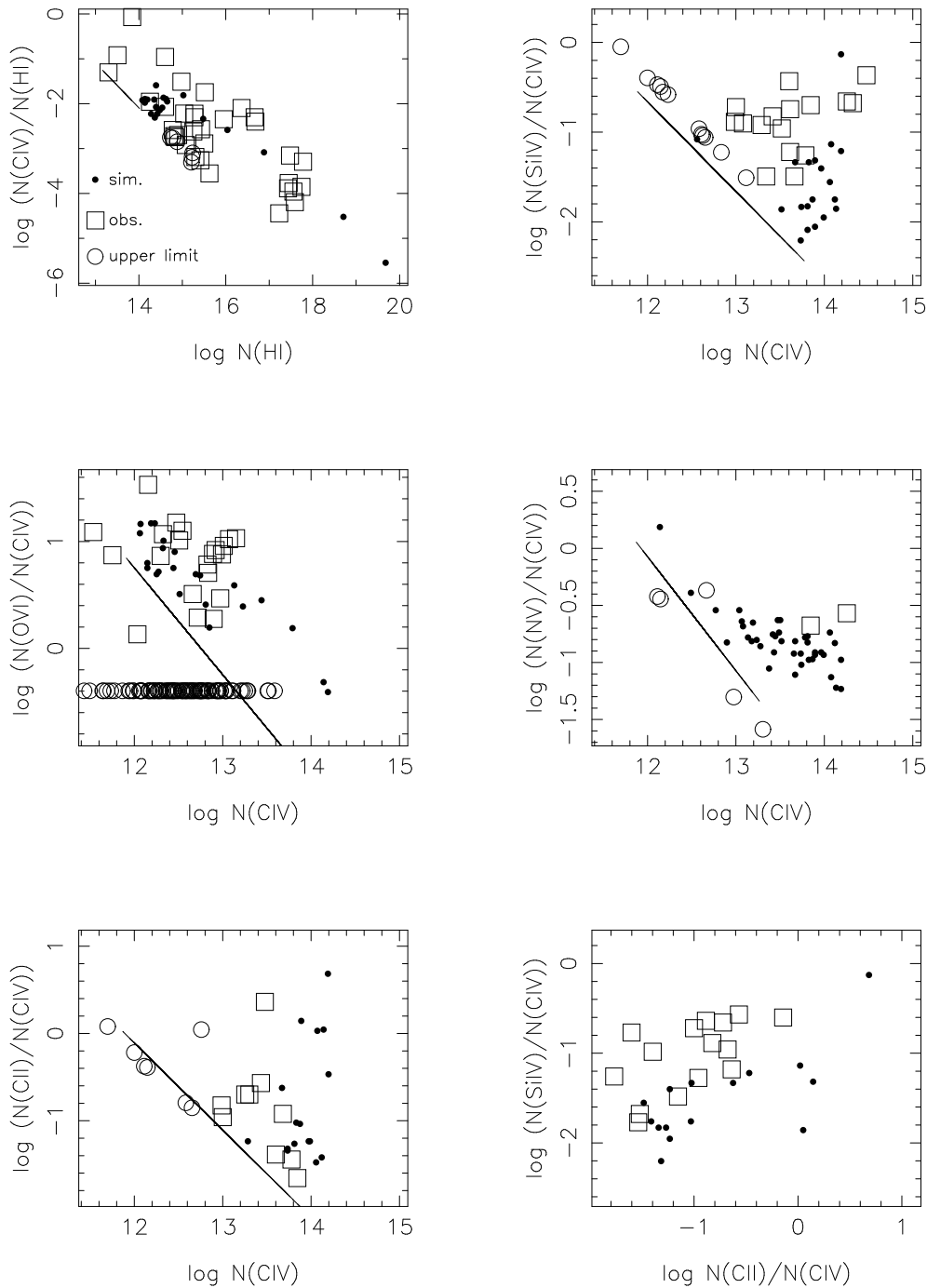


FIG. 12.—Column density ratios obtained from profile fitting the simulated data. An absolute metallicity $[Z/H] = -2$, solar relative abundances and power-law UV spectrum with $\alpha = 1.5$ and $J_{-2.2} = 3$ were assumed. Filled circles denote the ratios of the sums of the column densities of all individual components along a LOS detectable at the 4.75σ level. The thin diagonal lines give upper limits for the simulated lines in cases where only one ion (H I in the first panel and C IV in the other cases) has been detected. Open squares mark observed values (see text); open circles, either observational upper limits or (bottom left-hand panel) O VI values undetermined because of blending.

species with different atomic weights permit a decomposition into the contributions from thermal and nonthermal (bulk) motion. The precise nature of the decomposition depends, however, on the velocity distribution of the bulk motion.

For the simulations, the relative importance of the contributions to the line formation can be easily studied as we have full knowledge of the density and peculiar velocity field along the LOS. Here we proceed as follows: from a display of the overdensity along a line of sight, we choose

density peaks and denote the spatial limits on both sides of the peak where the density has dropped by about an order of magnitude with a cursor. A program then computes the column density-weighted temperature and rms velocity dispersion within the selected spatial regions. Then we fit the absorption line closest to the position of the velocity centroid of the region with a Voigt profile and compare results. The top panel in Figure 15 shows a plot of the “observed” C IV Doppler parameter from the fit versus the purely thermal Doppler parameter computed straight from the

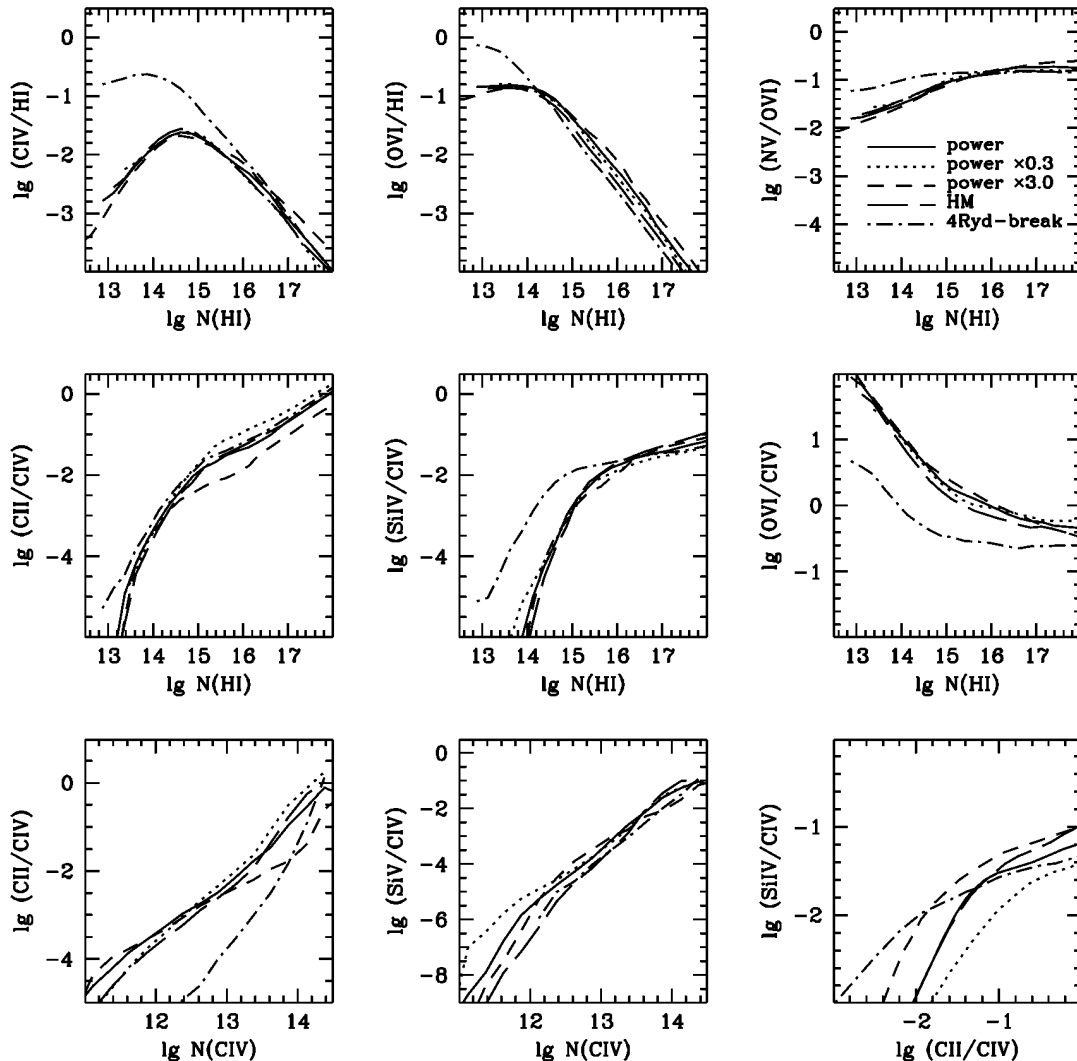


FIG. 13.—Column density ratios for various UV background radiation fields. The solid curve are for the $\alpha = 1.5$ power-law spectrum. The other curves are for a power law with intensity increased and decreased by factors of 3; a spectrum taking intergalactic absorption and emission into account (Haardt & Madau 1996); and a power law with a break at 4 ryd (flux reduced by a factor 100 at 4 ryd, constant flux for higher energies up to the point where the flux equals that of the underlying power law).

temperature array of the simulation. While the density-weighted thermal C IV Doppler parameter of many LOS hovers around $7\text{--}8\text{ km s}^{-1}$, the “observed” values occur over a wide range. The total C IV Doppler parameter is obviously not an unbiased measure of the temperature alone, as there are substantial, varying contributions from bulk motion. It is not obvious how temperature and bulk motion should be deconvolved. Making the simplest possible *Ansatz* of adding them in quadrature (which would be strictly true if the bulk motion followed a Gaussian velocity distribution), we arrive at the results shown in the lower panel: the observed line width does indeed measure the quadratic sum of thermal motion and rms velocity dispersion to a reasonable accuracy. Outliers in the plot are due to small spurious line components sometimes introduced by the semiautomatic fitting program VPFIT to improve the quality of the fit.

How realistic are the gas motions in the simulation? To compare the simulation to real data, we chose a number of randomly selected, simulated absorption lines for Voigt profile fitting. The resulting Doppler parameter column

density ($b\text{--}\log N$) diagrams for C IV, O VI, and H I are shown in Figure 16. The scatter plots are in very good qualitative agreement with those from observational data (see, e.g., Rauch et al. 1996 for C IV and Hu et al. 1995 for H I; there is no comparable information yet for O VI), as are the Doppler parameter distributions for simulated and observed C IV Doppler parameters (Fig. 17). The presence of a minimum b parameter for C IV and H I and a slight increase of $b_{\text{H I}}$ with $N(\text{H I})$ have both been observed. This agreement also holds for the decomposition into thermal and turbulent contributions to the Doppler parameter. Both total and thermal mean Doppler parameters are indistinguishable from the observed mean b values for H I and C IV (see Table 1). The observed mean thermal C IV Doppler parameter, $\langle b \rangle_{\text{therm}} = 7.2\text{ km s}^{-1}$, corresponds to $\sim 4 \times 10^4\text{ K}$.

Can we observe the infalling motion during gravitational collapse directly? Naively we may expect to see substantial line broadening due to infalling gas. However, the H I density-weighted velocity dispersion along the LOS (the physical quantity relevant for the line broadening) has a median as low as 11.6 km s^{-1} , even though the average

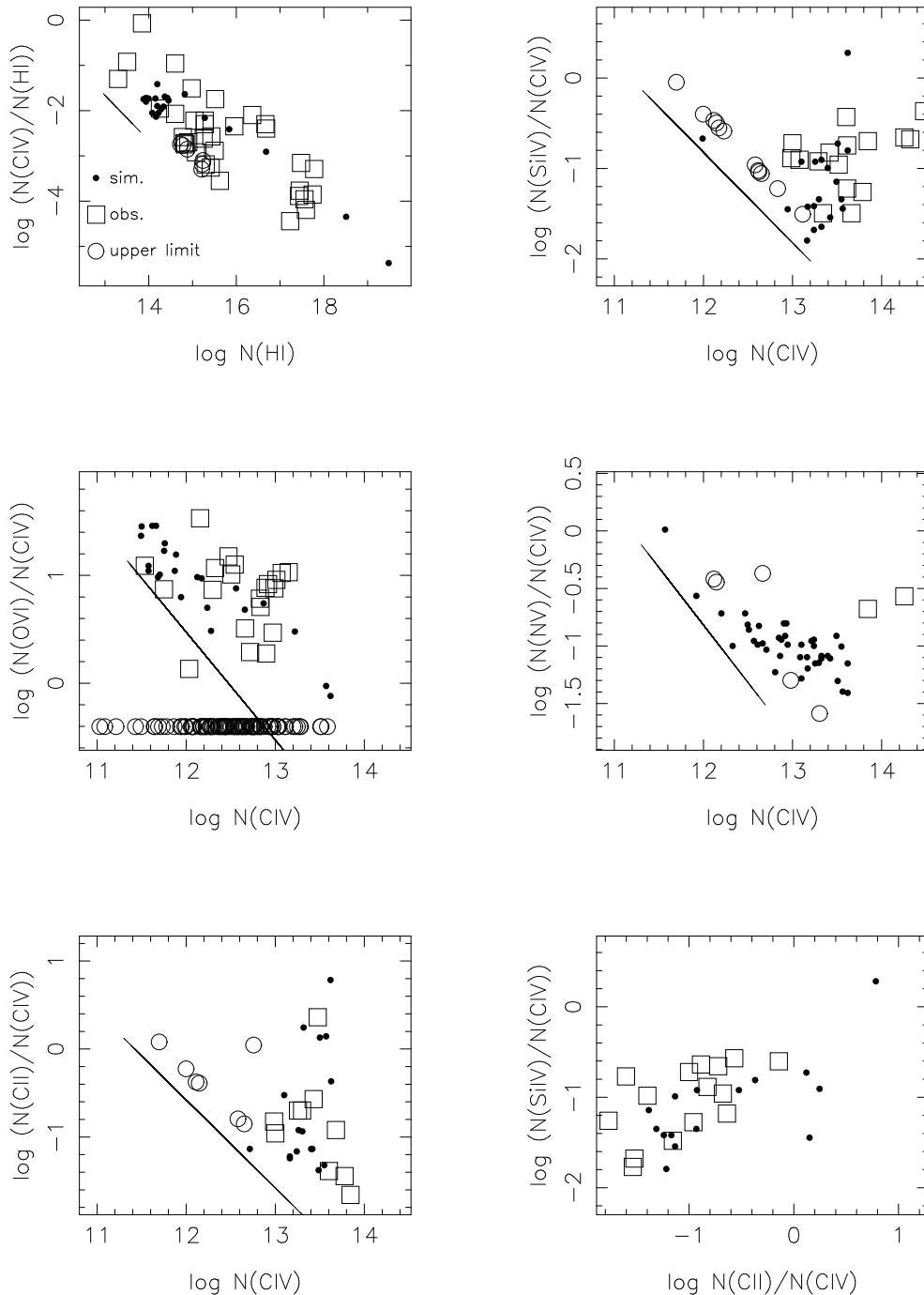


FIG. 14.—Column density ratios obtained from profile fitting the simulated data (*filled circles*). Compared to Fig. 12, the absolute metallicity has been changed from $[Z/H] = -2$ to -2.5 , solar relative abundances have been replaced by those of metal-poor stars ($[C] = [N] = 0$, $[Si] = [O] = 0.4$), and the spectrum suggested by Haardt & Madau (1996) is used instead of a power law with $\alpha = 1.5$. The diagonal lines give upper limits for the simulated absorption features in cases where only one ion (H I in the first panel and C IV in the others) has been detected. Open squares mark observed values (see text); open circles, either observational upper limits or undetermined O VI.

TABLE 1

| OBSERVED AND SIMULATED DOPPLER PARAMETERS | | | |
|---|------------------------------------|------------------------------------|--------------------------------------|
| PARAMETER | H I 1216 Å | C IV 1548 Å | |
| | $\langle b \rangle_{\text{total}}$ | $\langle b \rangle_{\text{total}}$ | $\langle b \rangle_{\text{thermal}}$ |
| Simulated | 27.3 | 8.6 | 7.7 |
| Observed | 28.0 ^a | 9.3 ^b | 7.2 ^b |

^a Hu et al. 1995.

^b Rauch et al. 1996.

radius of the regions used for the computation of this quantity was as large as 40 kpc. Looking at the peculiar velocity diagrams in Figures 4 and 5 with their large velocity gradients of close to 200 km s^{-1} across the size of a PGC, the quiescent structure may be somewhat surprising. However, the enhanced density responsible for the line formation is strongly peaked on a spatial scale much smaller than the infalling region. The line profile samples mostly the high-density gas that has gone through the shock front, has

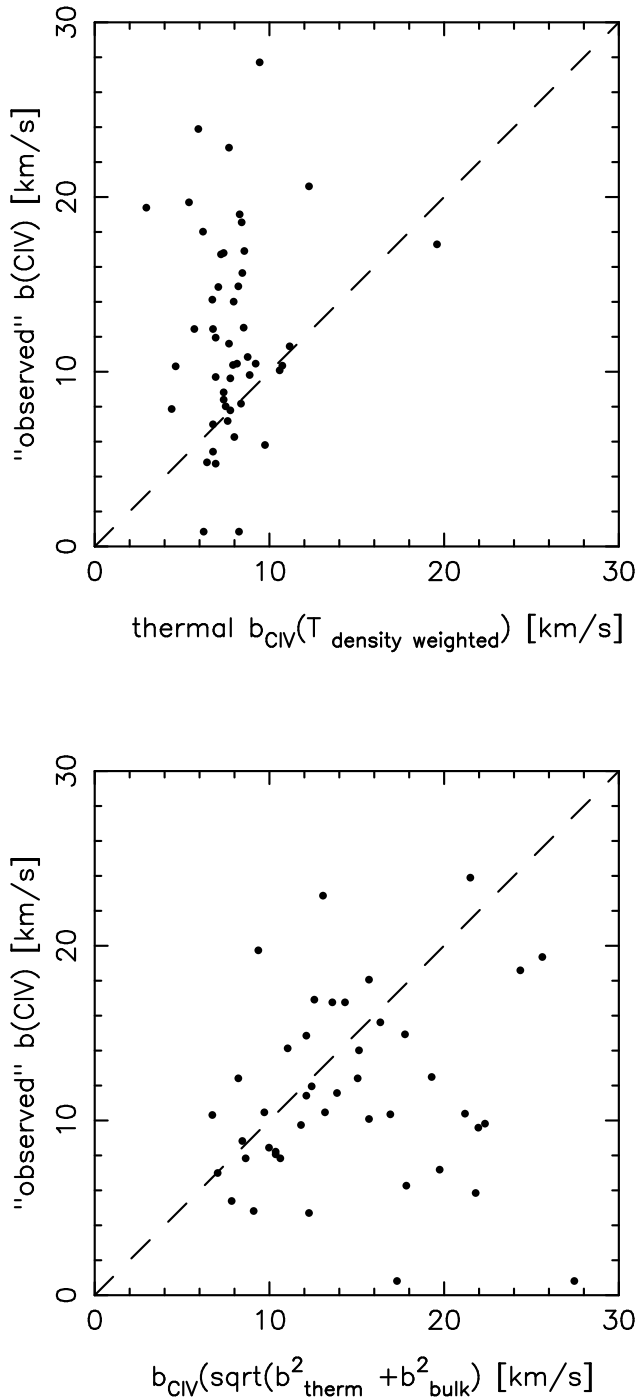


FIG. 15.—Upper panel: Total C IV Doppler parameter measured by profile fitting vs. density-weighted C IV thermal Doppler parameter computed from the gas temperature in the simulation. Lower panel: Total measured C IV Doppler parameter vs. the Doppler parameter obtained by adding RMS bulk velocity dispersion and thermal velocity dispersion in quadrature.

cooled to temperatures of a few 10^4 K, and is more or less at rest. In principle, the signature of infalling gas is still visible in the form of broad profile wings. In C IV, however, these are almost always too weak to be seen, as they are due to low column density gas beyond the radius of the shock. The situation may be different for H I absorption lines (see Rauch 1996). In O VI with its much larger cross section and

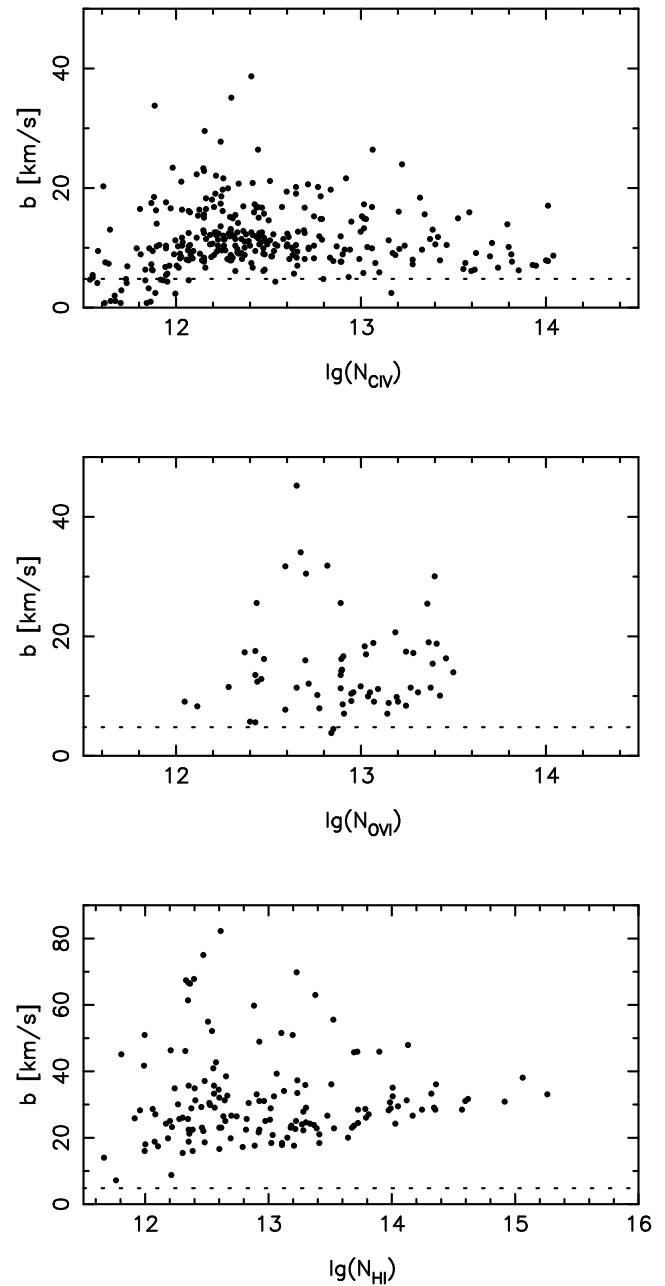


FIG. 16.—Doppler parameter–column density (b – $\log N$) diagrams for C IV (top), O VI (middle), and H I (bottom). The dotted lines give the spectral velocity resolution. Note the different scales of the axes.

weaker density dependence, we probably also have a better chance to detect infall. The O VI Doppler parameter ($\langle b \rangle_{\text{sim}} = 11.5 \text{ km s}^{-1}$) is indeed higher than that of C IV, and not lower, as one could naively expect for thermally dominated gas. Obviously the O VI–absorbing gas is subject to stronger nonthermal motions.

How do the Doppler parameters vary as a function of impact parameter? The LOS-integrated temperature distribution of either C IV or O VI does not show a radial variation that could be used as a measure of the impact parameter. This is due to the fact that some of the absorption components are related to different PGCs. Plotting, however, only the Doppler parameters of the strongest absorption component in each C IV complex (Fig. 18, top

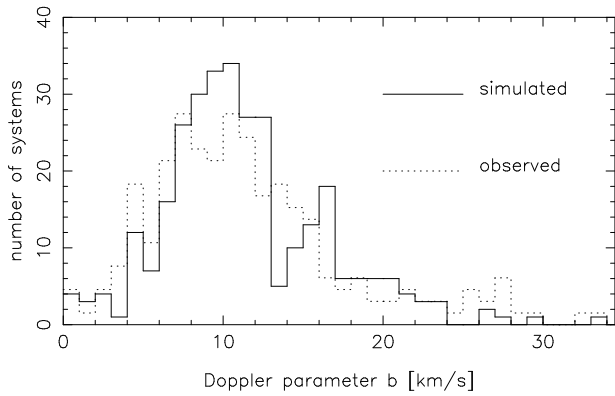


FIG. 17.—Comparison between the C IV Doppler parameters from the simulation (solid line) and the observed distribution from Rauch et al. (1996) (dotted line). The observed distribution has been scaled so as to match the total number of lines of the simulated distribution.

panel), we obtain a noticeable anticorrelation of $b(\text{C IV})$ with impact parameter from the center of the closest PGC. This seems to reflect the drop in temperature (bottom panel) and the coming to rest of the gas at small radii (< 12 kpc in this case). The trend is not obvious for O VI (not shown here), which arises from a much larger region of lower density. It

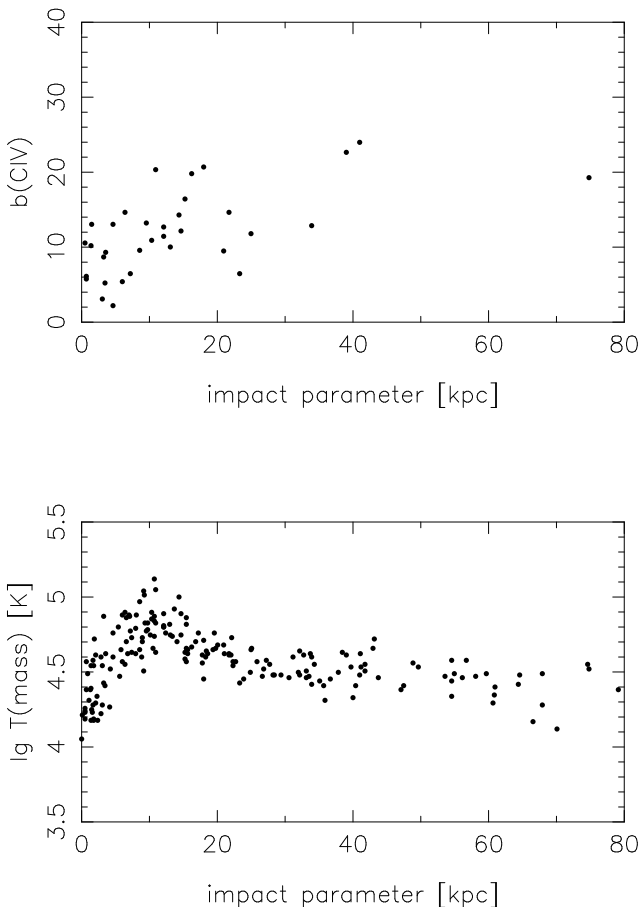


FIG. 18.—Doppler parameters of strongest C IV line of each absorption complex as a function of impact parameter to the nearest PGC (top); mass-weighted temperature (bottom).

also does not show up in plots of $b(\text{C IV})$ when all components, rather than the strongest in each complex, are considered.

4.3. The Two-Point Correlation Function (TPCF) and the Dynamical State of the Absorbers on Large Scales

As discussed earlier, the observed velocity spreads among absorption components are difficult to reconcile with an entirely dynamical velocity dispersion. In Paper I, it was suggested that the occasional large velocity splitting of sometimes more than 1000 km s^{-1} can be explained by chance alignments of the LOS with filaments containing several PGCs.

The TPCF for the simulation box described earlier (containing three $v_c \sim 100 \text{ km s}^{-1}$ galaxies) is shown in the upper panel of Figure 19. The velocities of the C IV systems were obtained by Voigt profile fits to significant continuum depressions. The absolute normalization comes from the observed TPCF for three QSOs ($\langle z \rangle = 2.78$; Rauch et al. 1996). Similar to the observed TPCF, the correlation function of C IV lines in the simulated spectra exhibits a narrow peak at the origin (the lowest velocity bin is incomplete) and a long tail out to velocities of $500\text{--}600 \text{ km s}^{-1}$ and beyond. The overall width is somewhat smaller than that of the observed distribution. Repeating the analysis for another

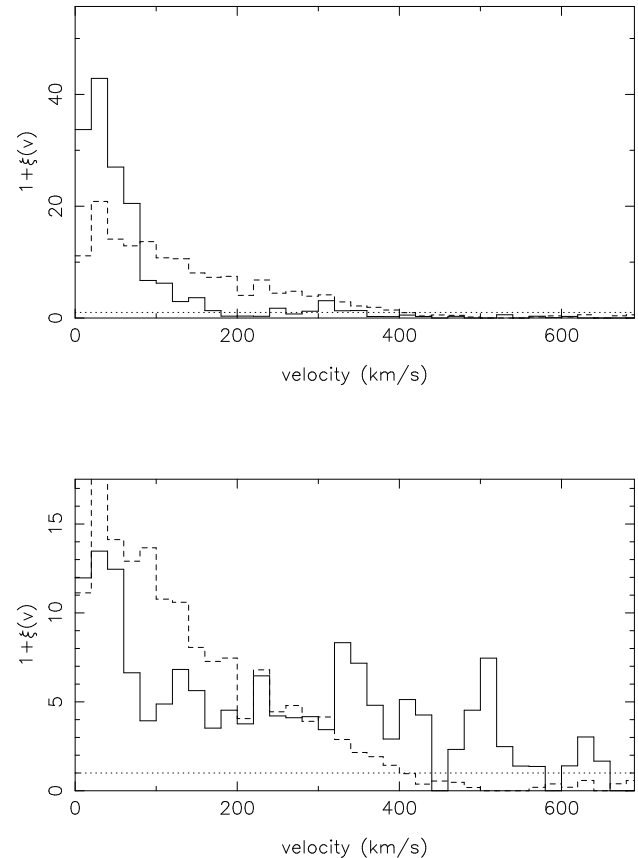


FIG. 19.—Upper panel: Two-point correlation function for the C IV systems detected in a simulation box at $z = 3.07$ (to contain three galaxies with $v_c \sim 100 \text{ km s}^{-1}$ at $z = 0$). Normalization is by the combined TPCF from the observations of three QSOs ($\langle z \rangle = 2.78$; Rauch et al. 1996). Lower panel: Same as above for a simulation box containing a single galaxy with $v_c \sim 200 \text{ km s}^{-1}$ by $z = 0$. Note the different scales of the axes.

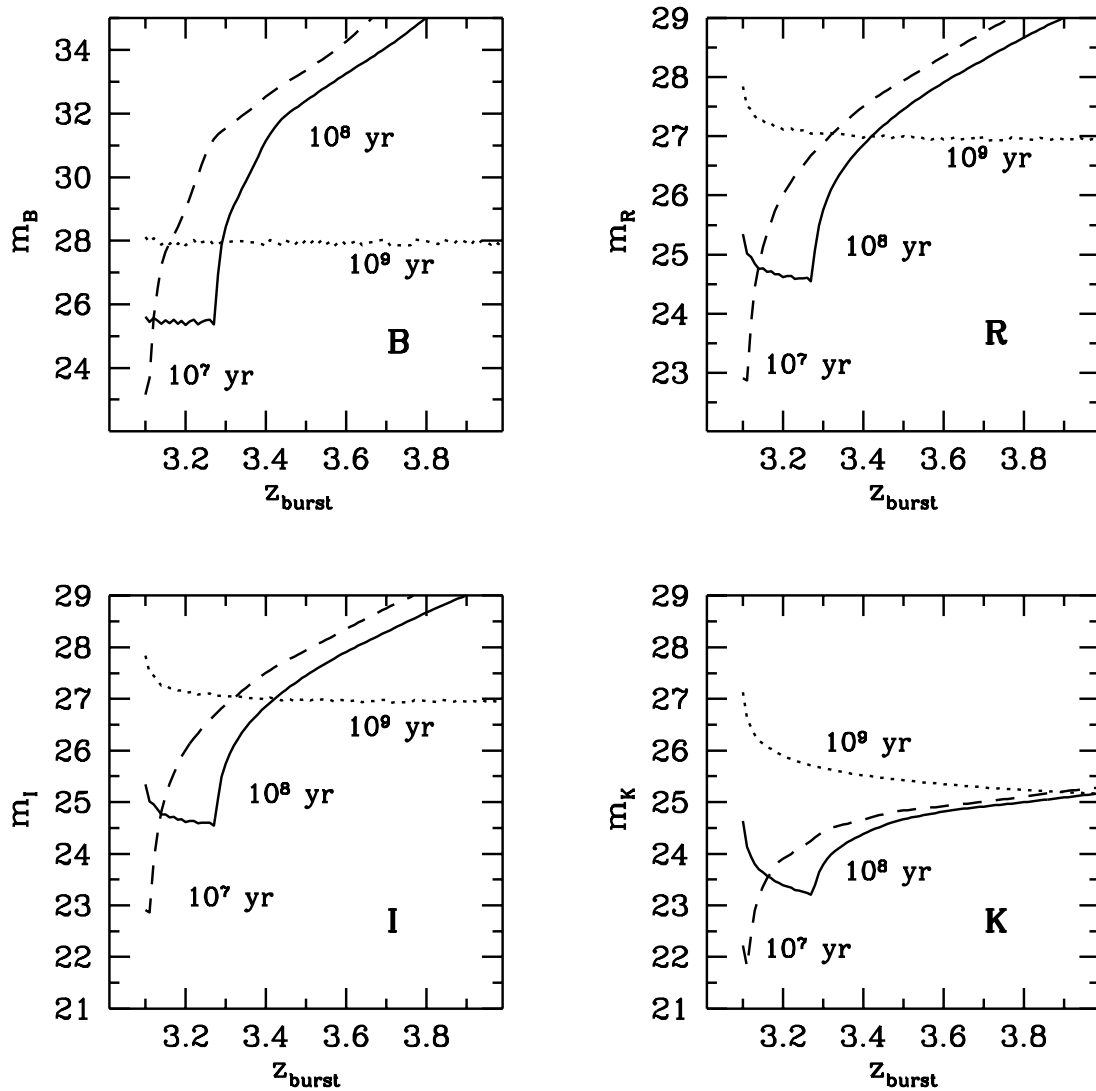


FIG. 20.—Bruzual & Charlot models for the apparent brightness (not corrected for Ly α and dust absorption, Salpeter IMF, or solar metallicity) at $z = 3.1$ for a total gas mass of a protogalactic clump of $10^9 M_{\odot}$, as a function of the redshift where star formation began. Different line styles indicate star formation timescales between 10^7 and 10^9 yr. Different panels are for different Johnson filters.

simulation box containing one galaxy with $v_c \sim 200$ km s^{-1} , we obtain the TPCF shown in the lower panel of Figure 19, which has much more power on large scales. Considering the rather small size of our simulation boxes, such variations from box to box are not surprising. In fact, the observed TPCF is also subject to a large scatter from QSO to QSO, as some LOS often contain only one or a few systems providing large velocity splittings. It seems plausible that the observed TPCF can be explained by averaging over TPCFs from individual galaxy-forming regions.

As for the origin of the large separations, splittings larger than those expected from the potential wells present ($\Delta v < 200\text{--}300$ km s^{-1}) must be due to additional contributions from large-scale motions. First, there is the expansion of the filamentary structure with the Hubble flow. There will be additional streaming motions of matter toward the massive knots connecting filaments (leading to the apparent “super-Hubble” expansion seen in Fig. 4b). Because of the small statistics involved, we have to await future studies to quantify the relative importance of the various effects.

As a formal measure of the velocity dispersion of an individual protogalactic region, we can compute the mean (over all LOS) of the rms of the density-weighted total velocity

$$\sigma_v = \left\langle \sqrt{\frac{\int (\bar{v} - v)^2 dn}{\int dn}} \right\rangle_{\text{LOS}}, \quad (3)$$

where $v = H(z)r + v_{\text{pec}}$, and

$$\bar{v} = \frac{\int v dn}{\int dn}. \quad (4)$$

For the standard box, with three future galaxies, $\sigma_v = 100$ km s^{-1} . Four other boxes developing into single ~ 200 km s^{-1} galaxies give $\sigma_v = 142, 134, 111,$ and 138 km s^{-1} .

4.4. Metal Absorbers in Emission

The observational identification of C IV absorbers at redshifts $z > 2$ with any known type of galaxies has proved difficult. Speculating that the absorbers may be related to

luminous galaxies with an old population of stars, Aragon-Salamanca et al. (1994) have obtained K images of QSO sight lines with known strong C IV absorbers to a K -limiting magnitude of 20.3. A slight excess of objects probably at the redshift of the QSO was found, but convincing identifications of individual absorbers were not possible.

Here we will briefly consider stellar population synthesis models (Bruzual & Charlot 1993; Charlot 1996) to investigate the prospects of detecting the stellar continuum from the PGCs responsible for the metal absorption systems in our model (see also Katz 1992; Steinmetz 1996a). We assume that the available gas turns into stars on timescales between 10^7 and 10^9 yr, a time span capturing the range from a short burst to extended star formation. In Figure 20, the apparent brightness (not corrected for Ly α and dust absorption) at $z = 3.1$ is shown for a total gas mass of $10^9 M_\odot$ (typical for a PGC) and three different star formation timescales as a function of the redshift where star formation began.

Figure 20 shows that our model would explain the non-detection of C IV absorbers in K by Aragon-Salamanca et al. (1994). Even a very short burst of $10^9 M_\odot$ reaches a peak K magnitude of only 21. Extended star formation reduces the maximum K magnitude to 25. A gas/star mass $\gtrsim 10^{11} M_\odot$ would be necessary to be permanently detectable in K from the ground.

However, if galaxies start building up at redshifts $z \sim 3$ by merging of smaller objects, recent star formation should have occurred at these redshifts. The optical passbands are then much more promising for a ground based detection of the stellar continuum. Figure 20 suggests that with *Hubble Space Telescope* (*HST*), the stellar continuum should be detectable in all wave bands redward of the Lyman break. Spectroscopic identification will be possible for only the most massive objects in the case of extended star formation and for a fraction of bursting PGCs of average mass if the star formation timescale is short. Recently, Steidel et al. (1996) and Giavalisco, Steidel, & Macchetto (1996) have reported the detection of a population of star-forming galaxies at comparable redshifts. It is intriguing that these objects could be identical to either a bursting fraction of average mass ($10^9 M_\odot$) objects or to the high-mass end of the population of PGCs, showing extended star formation (Steinmetz 1996a).

Finally, one should note that confusion with foreground galaxies is a concern when studying regions of ongoing galaxy formation as described in this paper. The inner 700 kpc of our simulation box (at $z = 3$) shown in Figures 1 and 3 correspond to an angular size slightly larger than that of an individual WFPC2 field. Thus, images as large as the full Hubble deep field may be required to get a “complete” picture of the progenitors of an individual large $z = 0$ galaxy. Superposition effects are then obviously quite severe.

5. DISCUSSION AND CONCLUSIONS

Gravitationally driven density fluctuations in a universe with hierarchical structure formation can explain QSO absorption phenomena at $z \sim 3$ over a wide range of column densities. While neutral hydrogen shows a rather tight correlation between column density and total density over a density range from 10^{-6} to 10^{-1} cm^{-1} , other ionic species probe different density and temperature regimes in a way specific to each species. The lowest H I column den-

sities (10^{12} – 10^{14} cm^{-2}) arise from large-scale sheetlike density enhancements in the IGM with an overdensity of only a few compared to the mean density of the universe. In this diffuse gas (densities around 10^{-5} cm^{-3}), high-ionization species are prevalent, and O VI $\lambda 1031$ is often the strongest metal absorption line. Toward higher H I column densities, we start probing filaments embedded in the large-scale sheets. In these regions, low column density C IV $\lambda\lambda 1548, 1550$ lines from infalling gas with densities around 10^{-4} cm^{-2} (overdensities of about 10–100) dominate the metal absorption features. C IV remains the most easily visible metal ion in the as yet unvirialized regions around the protogalactic clumps that are later to merge into present-day galaxies. Still larger H I column densities occur for lines of sight approaching the central regions of PGCs. These give rise to Lyman limit systems and eventually to damped Ly α absorbers. Total densities here exceed 10^{-4} cm^{-3} , and species like C II and Si IV become increasingly prominent. At densities above 10^{-3} cm^{-3} , we have reached the virialized region that is generally optically thick for radiation shortward of 1 ryd.

Although current simulations cannot precisely constrain the size of the damped region in a PGC, the fact that at $z \sim 3$ more than 10 such objects exist in the comoving volume containing one L_* galaxy at $z = 0$ considerably reduces the cross section per object required to explain the observed rate of incidence of damped Ly α absorbers. If this picture is correct, there should be no 1:1 correspondence between present-day galaxies and high-redshift damped (or Lyman limit) absorbers. There is then no need for hypothetical large disks/halos as high redshift progenitors of $z = 0$ galaxies.

The analysis of artificial spectra generated from our numerical simulation was carried out using the same methods as for observational data. The results are in remarkable quantitative agreement with a number of observed properties:

The predicted shape of the H I column density distribution shows good agreement with that of the observed distribution, and a good fit is obtained for $[\Omega_b/(0.05 h_{50}^2)]^2/(J_{-22} h_{50}) \approx 0.7$. Detailed information on the strength of accompanying metal absorption has recently become available for H I column densities as small as a few times 10^{14} cm^{-2} . We obtain good overall agreement between the results from our artificial spectra and the observed properties, either with a simple power-law UV spectrum ($\alpha = 1.5$, $J_{-22} = 3$) or with the spectrum proposed by Haardt & Madau (1996). This seems consistent with the lower end of the range of J values measured from the proximity effect (see, e.g., Giallongo et al. 1996, and references therein) and suggests a baryon fraction slightly exceeding the nucleosynthesis constraint (Walker et al. 1991).

The scatter of the column density ratios for Si IV/C IV, C II/C IV, and O VI/C IV versus C IV is consistent with the observational results, so the range of ionization conditions appears to be well captured by the simulations.

As is already apparent from simple photoionization models, the observed metal line strength corresponds to a mean metallicity $[C/H] = -2.5$ for the column density range 10^{14} – 10^{17} cm^{-2} . A homogeneous metal distribution reproduces the observed ion ratios well. This implies that much of the as yet unvirialized gas had been subject to a widespread phase of stellar nucleosynthesis well before

$z = 3$, and we are seeing the infall of gas that is already metal contaminated. Alternatively, there may be efficient, current metal transport outward from the PGCs.

Nevertheless, the observed scatter in $[C/H]$ is larger by a factor 3–10 than predicted by our numerical simulations where the metals were distributed homogeneously. This may indicate that some of the metal enrichment took place in situ with incomplete mixing prior to observation. In reality, there may also be a wider spread in physical conditions (e.g., spatial variations of strength and spectrum of the UV field) than assumed by the simulations.

The observed column density ratios are matched significantly better if we use relative abundances appropriate for metal-poor stars (we used $[C] = [N] = 0$ and $[Si] = [O] = 0.4$). Damped Ly α systems at redshifts >3 show similar low metal abundances ($-2.5 < [Z/H] < -2.0$) and relative metallicities (Lu et al. 1996, and references therein). This is consistent with the idea that metal absorption systems at high redshift contain a record of early nucleosynthesis dominated by supernovae of Type II.

The observed distribution of Doppler parameters and the relative contributions to the line width from thermal and nonthermal motion are well reproduced by the simulations. Obviously, shock heating is a second important heating agent (in addition to photoionization heating) for regions of the universe with overdensities between 10 and a few hundred. In spite of the large peculiar velocities ($\sim 100 \text{ km s}^{-1}$) of the infalling gas, C IV absorption lines are typically only $\sim 8\text{--}10 \text{ km s}^{-1}$ wide. This is because the C IV optical depth arises mostly in narrow postshock regions where the shocked gas has already come to rest and is cooling rapidly. Bulk motion contributions to the Doppler parameters for O VI and H I are larger because much of the absorption arises at larger impact parameters, where infall of gas is a more important broadening agent. In the particular model of structure formation investigated here, the C IV Doppler parameter is, to a good approximation, measured by the quadratic sum of the thermal and the rms bulk velocity dispersion.

The large-scale structure in velocity space, as measured by the C IV TPCF, is consistent with the observed C IV TPCF. This supports the hypothesis proposed in Paper I that LOS that intersect expanding large-scale filaments with embedded PGCs contribute significantly to the high velocity-tail of the C IV TPCF. On smaller scales ($\Delta v < 300 \text{ km s}^{-1}$), we may be seeing genuine spatial clustering, the velocity dispersion internal to individual PGCs, and streaming motions within filaments. A hypothetical class of abundant, deep potential wells at high redshift may not be required.

We have discussed the prospects of detecting the stellar continuum that is expected from protogalactic clumps if at least some metal enrichment has occurred in situ. These objects should be visible at all optical wavelengths in deep images with *HST* and in all optical passbands from the ground, at least longward of the Lyman break. We also suggested to interpret the Lyman break objects at redshifts around 3 reported by Steidel et al. (1996) in terms of the high-mass end of the PGCs causing metal absorption systems or of a bursting fraction of lower mass PGCs.

Prospects for identifying metal absorption systems at these redshifts are good. The best strategy seems to be a systematic search for Lyman break objects within a few arcseconds to the line of sight to quasars, together with follow-up spectroscopy to the faintest possible limits. PGCs that are progenitors of a particular $z = 0$ galaxy can be scattered over several hundred kpc at $z = 3$, an area larger than the field size of the *HST* WFPC2 camera, so problems with incompleteness and foreground confusion can arise.

Substantial simplifications are present in the current work; in particular, additional structure on mass scales below our resolution limit may occur. In the future, a large database of metal-line ratios as a function of redshift should improve constraints on the normalization and spectrum of the UV background and should allow us to distinguish between possible metal enrichment histories of the IGM. In particular, in the low-density regions probed by the lowest column density Ly α absorbers, we expect O VI to be considerably stronger than C IV. Thus, it may be possible to push metallicity determinations with O VI closer to truly primordial gas than is possible with C IV, despite the severe problems with identifying O VI in the Ly α forest. Another interesting case for further study is Si IV. Si IV should rapidly decrease toward low densities, and a detection in low H I column density systems would indicate that the normalization and/or the spectrum of the UV background differ significantly from those we have adopted. Studying the redshift evolution of the C IV velocity space correlation function may help to test the picture of hierarchical clustering.

A detection of the stellar continuum expected to be associated with metal absorption systems at kpc separations from QSO lines of sight would allow us to investigate the radial and metallicity profile of the PGCs.

In summary, we have found that high-resolution hydrodynamical simulations of galaxy-forming regions can substantially aid the interpretation of the observed properties of metal absorption systems. Currently, these simulations are best suited for studying regions with overdensities from 10 to a few hundred. Such regions are optically thin to ionizing radiation.

The good and sometimes excellent agreement of the present model with observation gives reason to believe that we have correctly identified the main mechanism underlying many of the metal absorption systems at high redshift; conversely, we may take the results presented here as an argument in favor of a hierarchical galaxy formation scenario.

We thank Bob Carswell and John Webb for VPFIT, and Gary Ferland for making CLOUDY available to us. Len Cowie, Limin Lu, Andy McWilliam, Wal Sargent, and Simon White have provided useful discussions and comments. We thank Jordi Miralda-Escudé for a helpful referee report. M. R. is grateful to NASA for support through grant HF-01075.01-94A from the Space Telescope Science Institute, which is operated by the Association of Universities for Research in Astronomy, Inc., under NASA contract NAS5-26555. Support by NATO grant CRG 950752 and the ‘‘Sonderforschungsbereich 375-95 für Astro-Teilchenphysik der Deutschen Forschungsgemeinschaft’’ is also gratefully acknowledged.

REFERENCES

- Aragon-Salamanca, A., Ellis, R. S., Schwartzberg, J.-M., & Bergeron, J. A. 1994, *ApJ*, 421, 27
- Bahcall, J. N. 1975, *ApJ*, 200, L1
- Bahcall, J. N., & Spitzer, L. 1969, *ApJ*, 156, L63
- Bechtold, J., Green, R. F., & York, D. G. 1987, *ApJ*, 312, 50
- Bergeron, J. 1986, *A&A*, 155, L8
- . 1995, in *QSO Absorption Lines*, Proc. ESO Workshop, ed. G. Meylan (Heidelberg: Springer), 127
- Bergeron, J., & Stasinska, G. 1986, *A&A*, 169, 1
- Bruzual, G., & Charlot, S. 1993, *ApJ*, 405, 538
- Burbidge, G., O'Dell, S. L., Roberts, D. H., & d Smith, H. E. 1977, *ApJ*, 218, 33
- Carswell, R. F., Webb, J. K., Baldwin, J. A., & Atwood, B. 1987, *ApJ*, 319, 709
- Cen, R., Miralda-Escudé, J., Ostriker, J. P., & Rauch, M. 1994, *ApJ*, 437, L9
- Chaffee, F. H., Foltz, C. B., Bechtold, J., & Weymann, R. J. 1986, *ApJ*, 301, 116
- Chaffee, F. H., Foltz, C. B., Röser, H. J., Weymann, R. J., & Latham D. W. 1985, *ApJ*, 292, 362
- Charlot, S. 1996, in *ASP Conf. Proc. 98, From Stars to Galaxies*, ed. C. Leitherer, U. Fritze-von Alvensleben, & J. Huchra (San Francisco: ASP), in press
- Churchill, C. W., Steidel, C. C., & Vogt, S. S. 1996, *ApJ*, 471, 164
- Cowie, L. L., Songaila, A., Kim, T.-S., & Hu, E. 1995, *AJ*, 109, 1522
- Davidson, A. F., Kriss, G. A., & Zheng, W. 1996, *Nature*, 380, 6569
- Djorgovski, S. G., Pahre, M. A., Bechtold, J., & Elston, R. 1996, *Nature*, 382, 6588
- Donahue, M., & Shull, J. M. 1991, *ApJ*, 383, 511
- Fall, S. M., & Rees, M. J. 1985, *ApJ*, 298, 18
- Ferland, G. J. 1993, University of Kentucky Department of Physics and Astronomy Internal Report
- Giallongo, E., Cristiani, S., D'Odorico, S., Fontana, A., & Savaglio, S. 1996, *ApJ*, 466, 46
- Giavalisco, M., Steidel, C. C., & Macchetto, D. 1996, *ApJ*, 470, 189
- Gingold, R. A., & Monaghan, J. J. 1977, *MNRAS*, 181, 375
- Gunn, J. E., & Peterson, B. A. 1965, *ApJ*, 142, 1633
- Haardt, F., & Madau, P. 1996, *ApJ*, 461, 20
- Haehnelt, M. G., Rauch, M., & Steinmetz, M. 1996a, *MNRAS*, in press
- Haehnelt, M. G., Steinmetz, M., & Rauch, M. 1996b, *ApJ*, 465, L95 (Paper I)
- Hernquist, L., Katz, N., Weinberg, D. H., & Miralda-Escudé, J. 1996, *ApJ*, 457, L51
- Hu, E. M., Kim, T. S., Cowie, L. L., Songaila, A., & Rauch, M. 1995, *AJ*, 110, 1543
- Kauffmann, G. A. M. 1996, *MNRAS*, 281, 475
- Katz, N. 1992, *ApJ*, 391, 502
- Katz, N., Weinberg, D. H., Hernquist, L., & Miralda-Escudé, J. 1996, *ApJ*, 457, L57
- Lake, G. 1988, *ApJ*, 327, 99
- Lucy, L. 1977, *AJ*, 82, 1013
- Lanzetta, K. M., et al. 1991, *ApJS*, 77, 1
- Lanzetta, K. M., Bowen, D. V., Tytler, D., & Webb, J. K. 1995, *ApJ*, 442, 538
- Lu, L., Sargent, W. L. W., Barlow, T. A., Churchill, C. W., & Vogt, S. 1996, *ApJS*, 107, 475
- McGill, C. 1990, *MNRAS*, 242, 544
- McWilliam, A., Preston, G. W., Sneden, C., & Searle, L. 1995, *AJ*, 109, 2757
- Miralda-Escudé, J., Cen, R., Ostriker, J. P., & Rauch, M. 1996, *ApJ*, 471, 582
- Mo, H. J. 1994, *MNRAS*, 269, 49P
- Mo, H. J., & Miralda-Escudé, J. 1996, *ApJ*, 469, 589
- Møller, P., & Warren, S. J. 1995, in *Galaxies in the Young Universe*, ed. H. Hippelein, K. Meisenheimer, & H. J. Roeser (New York: Springer), 88
- Morris, S. L., Weymann, R. J., Foltz, C. B., Turnshek, D. A., Shectman, S., Price, C., & Boroson, T. A. 1986, *ApJ*, 310, 40
- Navarro, J. F., & Steinmetz, M. 1997, *ApJ*, in press
- Petitjean, P., & Bergeron, J. A. 1994, *A&A*, 283, 759
- Petitjean, P., Mückel, J. P., & Kates, R. E. 1995, *A&A*, 295, L9
- Petitjean, P., Webb, J. K., Rauch, M., Carswell, R. F., & Lanzetta, K. 1993, *MNRAS*, 262, 499
- Pettini, M., Hunstead, R. W., Murdoch, H. S., & Blades, J. C. 1983, *ApJ*, 273, 436
- Pettini, M., Smith, L. J., Hunstead, R. W., & King, D. L. 1994, *ApJ*, 426, 79
- Rauch, M. 1996, in *Cold Gas at High Redshift*, ed. M. Bremer, P. Van der Werf, & C. Carilli (Dordrecht: Kluwer), in press
- Rauch, M., Sargent, W. L. W., Womble, D. S., & Barlow, T. A. 1996, *ApJ*, 467, L5
- Rauch, M., et al. 1997, in preparation
- Sargent, W. L. W., Boksenberg, A., & Steidel, C. C. 1988, *ApJS*, 68, 539
- Sargent, W. L. W., Young, P. J., Boksenberg, A., Carswell, R. F., & Whelan, J. A. J. 1979, *ApJ*, 230, 49
- Savaglio, S., Cristiani, S., D'Odorico, S., Fontana, A., Giallongo, E., & Molaro, P. 1996, *A&A*, 137
- Songaila, A., & Cowie, L. L. 1996, *AJ*, 122, 335
- Steidel, C. C. 1990, *ApJS*, 74, 37
- . 1995, in *QSO Absorption Lines*, Proc. ESO Workshop, ed. G. Meylan (Heidelberg: Springer), 139
- Steidel, C. C., Giavalisco, M., Pettini, M., Dickinson, M., & Adelberger, K. L. 1996, *ApJ*, 462, L17
- Steinmetz, M. 1996a, in *The Universe at High Redshift with VLT*, Proc. ESO Workshop, ed. J. Bergeron, in press
- . 1996b, *MNRAS*, 278, 1005
- Sugimoto, D., Chikada, Y., Makino, J., Ito, T., Ebisuzaki, T., & Umemura, M. 1990, *Nature*, 345, 33
- Timmes, F. X., Woosley, S. E., & Weaver, T. A. 1995, *ApJS*, 98, 617
- Tyson, N. D. 1988, *ApJ*, 329, L57
- Tytler, D., Fan, X.-M., Burles, S., Cottrell, L., Davis, C., Kirkman, D., & Zuo, L. 1995, in *QSO Absorption Lines*, Proc. ESO Workshop, ed. G. Meylan (Heidelberg: Springer), 289
- Vedel, H., Hellsten, U., & Sommer-Larsen, J. 1994, *MNRAS*, 271, 743
- Viegas, S. M., & Gruenwald, R. B. 1991, *ApJ*, 377, 39
- Walker, T. P., Steigman, G., Schramm, D. N., Olive, K. A., & Kang, H. S. 1990, *ApJ*, 376, 51
- White, S. D. M., & Frenk, C. S. 1991, *ApJ*, 379, 52
- Wolfe, A. M. 1988, in *QSO Absorption Lines: Probing the Universe*, ed. C. Blades, C. Norman, & D. Turnshek (Cambridge: Cambridge Univ. Press), 297
- York, D. G., Dopita, M., Green, R., & Bechtold, J. 1986, *ApJ*, 311, 610
- Zhang, Y., Anninos, P., & Norman, M. L. 1995, *ApJ*, 453, L57